Journal of Hydrology: Regional Studies 34 (2021) 100783

Contents lists available at ScienceDirect

Journal of Hydrology: Regional Studies

journal homepage: www.elsevier.com/locate/ejrh

Numerical analysis of the potential for mixed thermal convection in the Buda Thermal Karst, Hungary

Márk Szijártó [a,*], Attila Galsa [a], Ádám Tóth [b], Judit Mádl-Szőnyi [b]

[a] Department of Geophysics and Space Science, ELTE Eötvös Loránd University, Budapest, Hungary
[b] Department of Geology, József & Erzsébet Tóth Endowed Hydrogeology Chair, ELTE Eötvös Loránd University, Budapest, Hungary

ARTICLE INFO

Keywords:
Heat transport mechanisms
Mixed thermal convection
Time-dependent thermal convection
Deep carbonate system
Finite element numerical modeling

ABSTRACT

Study region: Buda Thermal Karst system, Hungary.
Study focus: The pilot area has high geothermal potential characterized by prominent thermal anomalies, such as thermal springs and spas which tap the Triassic carbonate aquifers. Therefore, numerical simulations were carried out to examine the temperature field and flow pattern considering three successive heat transport mechanisms: thermal conduction, forced and mixed thermal convection in order to highlight the role of different driving forces of groundwater flow in the Buda Thermal Karst.
New hydrological insights for the region: Compared to thermal conduction, topography-driven heat advection increases the surface heat flux. The superimposed effect of free thermal convection facilitates the formation of time-dependent mixed thermal convection from the deep carbonate layers. The Nusselt number varied between $Nu = 1.56$ and 5.25, while the recharge rate (R) ranged from $R = 178$ mm/yr to 250 mm/yr. Radiogenic heat production and hydraulically conductive faults have only a minor influence on the basin-scale temperature field and flow pattern. Boundary conditions prescribed on the temperature and pressure can considerably affect the numerical results. In each scenario, independently of the model parameters, time-dependent mixed thermal convection evolved both in the deep and the confined parts of the karstified carbonates of the Buda Thermal Karst system.

1. Introduction

Today, renewable energy is of interest for supplying electrical and heating/cooling demands due to decreasing fossil resources and increasing greenhouse gases. In general, deep or shallow power plants, borehole heat exchangers (BHEs), enhanced geothermal systems (EGSs) and numerous other techniques are used to develop and exploit geothermal energy. For the optimal operation of these systems, the effects of various heat transport mechanisms in the subsurface must be understood (e.g. Arola et al., 2014). However, using the local-scale approximation might not always be an adequate method to study groundwater flow and heat transport mechanisms, for instance, in the case of a regional-scale aquifer system.

Basin-scale groundwater flow can be induced by the combined effect of different driving forces including water table configuration (e.g. Tóth, 2009; Jiang et al., 2018), sedimentary compaction (e.g. Cathles and Smith, 1983; Harrison and Summa, 1991), tectonic compression (e.g. Ge and Garven, 1992; Tóth and Almási, 2001), buoyancy forces by chemical composition (e.g. Simmons et al., 1999;

* Corresponding author.
E-mail address: mark.szijarto@ttk.elte.hu (M. Szijártó).

https://doi.org/10.1016/j.ejrh.2021.100783
Received 7 August 2020; Received in revised form 12 January 2021; Accepted 16 January 2021
Available online 11 February 2021

Voss et al., 2010) and heat transfer (e.g. Domenico and Palciauskas, 1973; Rabinowicz et al., 1998; Lopez et al., 2016).

In this paper, two-dimensional numerical modeling was used to focus on the interaction of topography- and thermal buoyancy-driven groundwater flow, while the effects of other driving forces were not considered. In the evaluation of heat transport processes, the role of topography-driven heat advection (forced thermal convection) (e.g. Domenico and Palciauskas, 1973; An et al., 2015) and thermal buoyancy (free thermal convection) (e.g. Lapwood, 1948; Lenkey, 1993) were investigated separately in theoretical models. If both forced and free thermal convection are acting on a flow system, the complex phenomenon is referred to as a mixed thermal convection (e.g. Cserepes and Lenkey, 2004; Yang et al., 2010; etc.). In this case the non-dimensional Rayleigh number cannot be used alone to describe the dynamics of the flow system. In a previous synthetic simulation study, Szijártó et al. (2019) revealed that appearance of time-dependent mixed thermal convection in a flow system depends on the non-dimensional Rayleigh and the modified Péclet number as functions of the model geometry, the permeability anisotropy, the water table slope and the geothermal gradient. Although higher geothermal gradients ($\nabla_z T > 30\ ^\circ$C/km) can facilitate the concurrent existence of heat advection and thermal buoyancy, a controversial question has remained partly open: can mixed thermal convection evolve in real groundwater flow systems, and if so, under what circumstances?

Effects of heat transport mechanisms have already been investigated in different types of aquifers using numerical simulations and field observation data. A regional-scale conductive transfer mechanism, for example, was shown in the deeper parts of the German Molasse Basin (Przybycin et al., 2017). However, the role of heat advection is more significant in highly permeable sediments. In the siliciclastic aquifers of the Rheingraben, mainly topography-driven forced thermal convection was suggested by Clauser and Villinger (1990). In the North German Basin, forced thermal convection was shown to drive the flow in the near-surface aquifers, while the additional effect of free thermal convection caused only local-scale temperature anomalies in thick sediments (Kaiser et al., 2011, 2013; Noack et al., 2013). Evidence for thermal convection was presented in the deep confined carbonate aquifer of the Po Plain, Italy (Pasquale et al., 2013), in the deep carbonate platform of Luttelgeest in the Netherlands (Lipsey et al., 2016), and in the geothermal carbonate reservoir of Hainaut in Belgium (Licour, 2014). The existence of mixed thermal convection was revealed by Lopez et al. (2016) in the siliciclastic formation of the Lake Chad Basin, where the blocks of the basin are separated by faults. Nevertheless, the intensity and the location of mixed thermal convection is influenced to varying degrees by faults/fractures (e.g. Yang et al., 2004; Malkovsky and Magri, 2016; Przybycin et al., 2017) and by the hydrogeological/geothermal properties (e.g. Dobson et al., 2003).

The flow processes of the Buda Thermal Karst (BTK) system in Hungary have been studied using various conceptual models (Vendel and Kisházi, 1964; Alföldi et al., 1968, 1981; Kovács and Müller, 1980). The significance of the interaction between unconfined and confined parts of the system was revealed by a two-dimensional, steady-state numerical simulation (Mádl-Szőnyi and Tóth, 2015). This study displayed the main flow systems (local, intermediate, regional), the temperature anomalies induced by advective heat transport and the different fluid components (meteoric-karst and saline-basinal). The geometry of the hydrogeological structure was responsible for the revealed asymmetric groundwater flow pattern which was strengthened by both hydraulic and hydrochemical data interpretation (Mádl-Szőnyi and Tóth, 2015, 2017; Erhardt et al., 2017). Different fluid components could be found in thermal springs of the study area (Erőss, 2010; Erőss et al., 2012).

In addition to the significant effect of forced thermal convection, an important contribution of free thermal convection was also

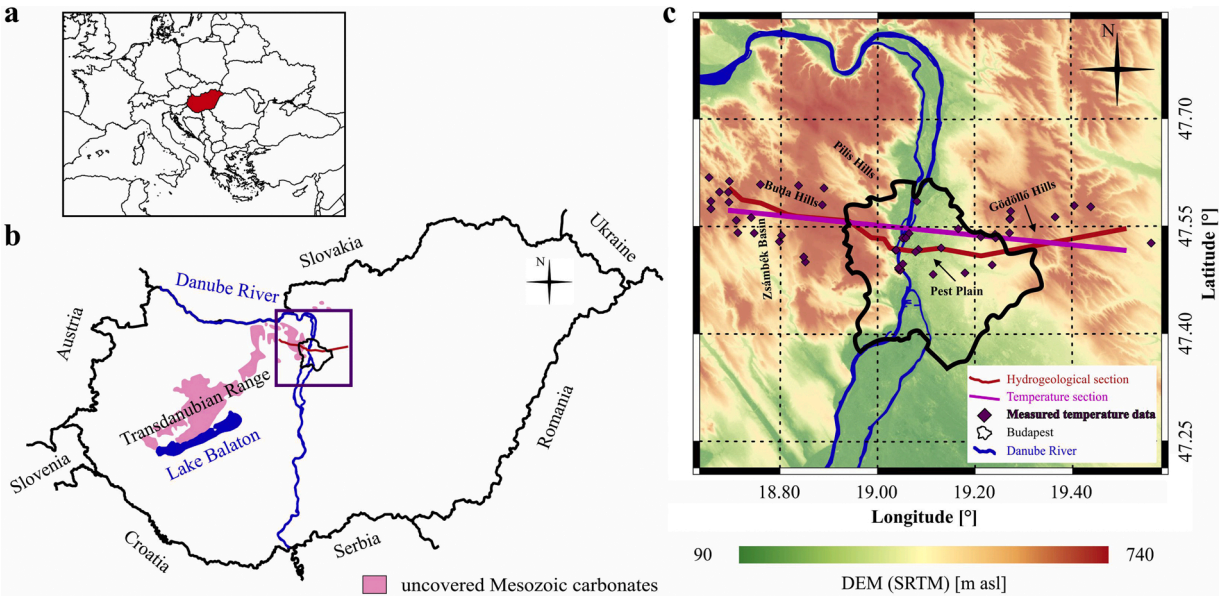

Fig. 1. (a) The location of Hungary in Europe, (b) the study area with the outcrops of the Mesozoic formations (magenta) (Tari et al., 1993; Haas, 2013; Máld-Szőnyi et al., 2019), and (c) the topography of the study area. The location of the hydrogeological cross-section (red) is shown (Appendix C - Supplementary data), and the temperature cross-section (magenta) with the projected temperature data was adopted from the Geothermal Database of Hungary (Dövényi, 1994).

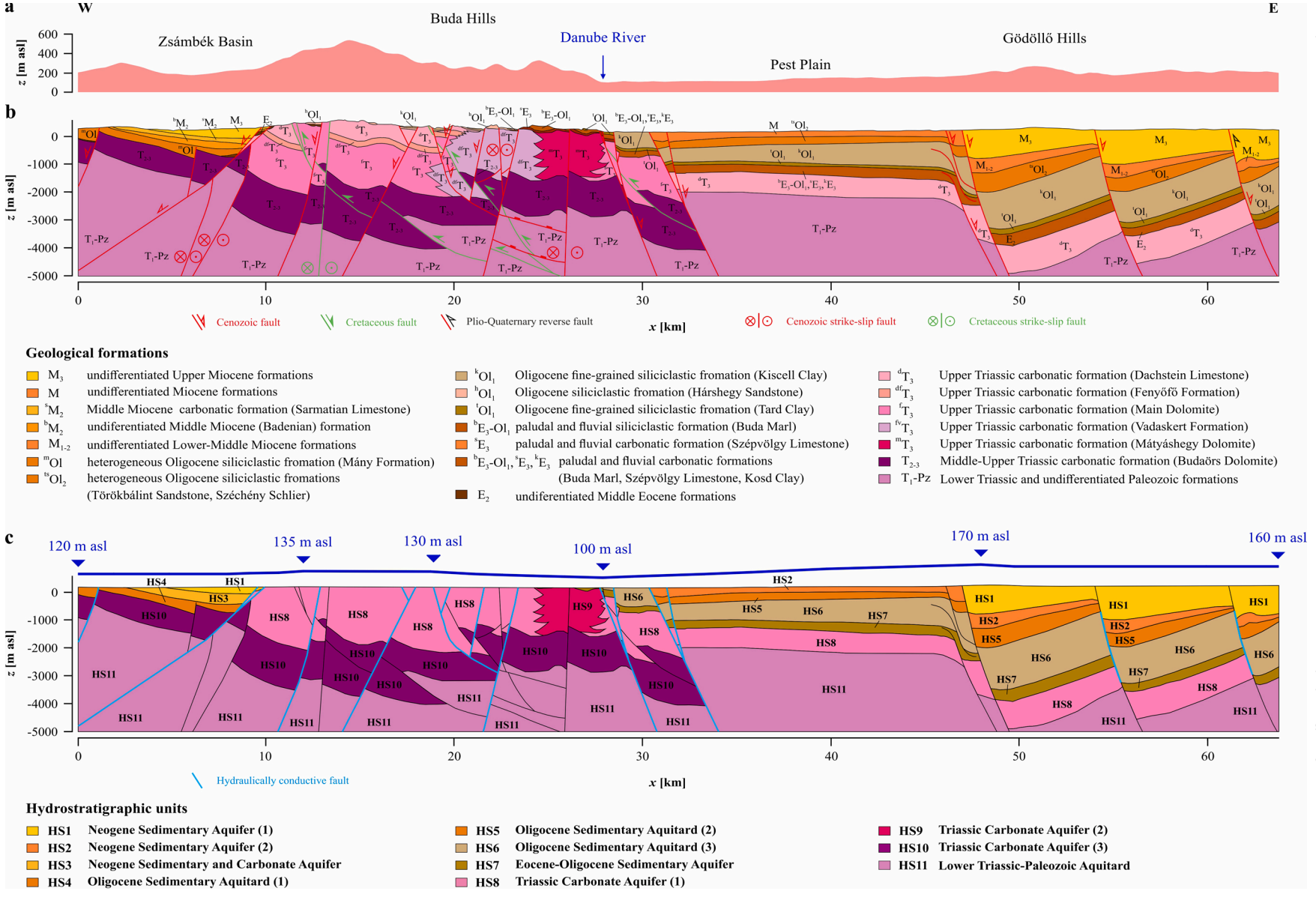

Fig. 2. (a) Topography along the two-dimensional section, (b) the geological section interpreted by Fodor (2011), and (c) the simplified hydrogeological section with the hydrostratigraphic units. Spatial variation of the water table elevation along the hydrogeological section based on measured data (Máld-Szőnyi et al., 2019; Mádl-Szőnyi, 2019). The vertical exaggeration is 1.5.

proposed in the conceptual model of Mádl-Szőnyi and Tóth (2015). Thermal convection was assumed important due to (1) the thickness of the carbonate aquifers (500–3000 m) (Goldscheider et al., 2010; Mádl-Szőnyi et al., 2018; Mádl-Szőnyi, 2019; Mádl-Szőnyi et al., 2018; 2019; Szijártó et al., 2019; etc.); (2) the high geothermal gradients ($\nabla_z T = 40$–$50\ ^\circ$C/km) (Dövényi and Horváth, 1988; Dövényi, 1994; Lenkey et al., 2002); and (3) the fluctuation in thermal water level in the caves of the BTK (Virág, 2019). As a next step, transient modeling was carried out to investigate the groundwater flow patterns and the temperature distributions in different evolutionary stages of the BTK based on simplified geology from the Late Miocene to present time (Havril et al., 2016; Havril, 2018). According to these studies, time-dependent mixed thermal convection was noticed in the earliest stage, when the Triassic carbonate was fully confined. However, comprehensive numerical simulations including coupled fluid flow and heat transport for the real hydrogeological settings have not yet been carried out in the region of the Buda Thermal Karst system of Hungary.

Over the course of our numerical simulations, the effects of three heat transport mechanisms on the groundwater flow pattern and the temperature distribution in the BTK were investigated using real hydrostratigraphic settings: (1) heat conduction, (2) forced convection and (3) mixed thermal convection. Further scenarios were also set up to examine the effect of hydraulically conductive faults, radiogenic heat production and boundary conditions on the temperature and fluid flow distribution. The recharge rate and the non-dimensional Nusselt number were calculated during the simulations in order to compare the numerical model with the measured precipitation and surface heat flux. Finally, the results of the numerical simulations were discussed and compared with the observed temperature data (Dövényi, 1994) using the approach suggested by Mádl-Szőnyi (2019), and other flow-related manifestations (e.g. Erőss, 2010; Erőss et al., 2012; Mádl-Szőnyi and Tóth, 2015; Mádl-Szőnyi et al., 2018; Virág, 2019; etc.).

2. Background of the basin-scale simulations

The Buda Thermal Karst (BTK) is located at the NE edge of the dominantly Mesozoic carbonate system of the Transdanubian Range. It is situated within and in the surroundings of Budapest, the capital of Hungary (Csepregi, 2007; Erőss et al., 2012; Mádl-Szőnyi et al., 2017). The topography of the study area varies as it includes lowlands and highlands (Fig. 1). The eastern region of the Transdanubian Range is the Buda Hills (559 masl) to the west of the Danube River. On the opposite side of the river, to the east, the Pest Plain (average elevation 210 masl) and Gödöllő Hills (344 masl) can be found (Fig. 2a). The annual mean temperature is 9.5–10 °C and annual rainfall is 500–600 mm (Marosi and Somogyi, 1990; Mersich et al., 2003).

The geometry of the simulated area is separated into two opposing half basins. The first is located to the west of the Danube River and the second can be found between the Danube and the Gödöllő Hills. Moreover, the geology of these two half-basins can be simplified into two main groups of hydrostratigraphic units: (1) an unconfined Mesozoic (mainly Triassic) carbonate sequence which is downfaulted and extends to the east and becomes (2) confined with a thick Neogene siliciclastic sedimentary cover (Haas, 1988, 2013; Haas et al., 2000, 2014; Fodor, 2011) (Fig. 2). For the goals of the numerical simulations, the complex geology and different lithological units were converted to 11 hydrostratigraphic units (HS) on the basis of a priori data and previous studies. These units were characterized by the necessary input physical parameters for the simulations (Fig. 2b and c; Bodri, 1981; Dövényi and Horváth, 1988; Rman and Tóth, 2011 (T-JAM project); Mádl-Szőnyi and Tóth, 2015, 2017; Havril et al., 2016; Békési et al., 2018; Mádl-Szőnyi et al., 2018, 2019; Tóth, 2018; Mádl-Szőnyi, 2019; Garamhegyi et al., 2020). Contrary to studies referring to karst systems, here we focused on the understanding of basin-scale flow patterns and heat transport processes. Therefore, the equivalent porous media (EPM) approach was used (e.g. Long et al., 1982; Scanlon et al., 2003; Abusaada and Sauter, 2012; Havril et al., 2016; Havril, 2018) assuming isotropic hydraulic conductivity in all hydrostratigraphic units.

The water table configuration follows the elevation of the topography on the eastern side of the area, while it is characterized by the karst water level on the western, unconfined side. Thus, the maxima of the water table elevation are 130 masl and 170 masl in the Buda Hills, and in the Gödöllő Hills, respectively (Máld-Szőnyi et al., 2019; Mádl-Szőnyi, 2019). The margin of the groundwater flow system is designated by the Danube River, which determines the regional minimum of the fluid potential ($h = 100$ masl) in the study area (Fig. 2c). The flow field is influenced and modified by normal, reverse and strike-slip faults both in the carbonates and the clastics (Fodor, 2011; Erhardt et al., 2017; Máld-Szőnyi et al., 2019).

3. Numerical model

3.1. Model description

The two-dimensional coupled fluid and heat transport simulations were carried out using the COMSOL Multiphysics® finite element simulation platform (version 5.2a) (Zimmermann, 2006), in order to investigate the interaction of different driving forces in the Buda Thermal Karst (BTK) system. The groundwater problem is described by the partial differential equation system including mass conservation, Darcy's Law and the heat transport equation (e.g. Nield and Bejan, 2017), which are given by

$$\varphi \frac{\partial \rho_w}{\partial t} + \nabla[\rho_w \mathbf{q}] = 0 \tag{1}$$

$$\mathbf{q} = -\frac{K}{\rho_w g}[\nabla p - \rho_w g\, \nabla z] \tag{2}$$

$$[\varphi\rho_w c_w + (1-\varphi)\rho_{ma} c_{ma}]\frac{\partial T}{\partial t} + \rho_w c_w \mathbf{q}\nabla T = \nabla\{[\varphi\lambda_w + (1-\varphi)\lambda_{ma}]\nabla T\} + Q_r \quad (3)$$

where **q**, p and T are the unknown Darcy flux, pressure and temperature, respectively. The physical parameters of the hydrostratigraphic units are listed in Table 1, while other model parameters are set out in Table 2. Although the uncertainties in the applied parameters can affect the results of the numerical simulations (Mishra et al., 2009; Foglia et al., 2013; Song et al., 2015), a global sensitivity analysis of input parameters cannot be carried out within the framework of the current study. Nevertheless, a simplified sensitivity analysis for the hydraulic and thermal conductivities is presented in Appendix A – Supplementary data. The water density, $\rho_w(T,p)$ depends on the temperature and the pressure (Magri, 2009).

The geometry of the numerical model is shown in Fig. 3a (thickness, $D = 5100$–5170 m; width, $L = 63.8$ km) including the boundary conditions applied in the base model (Model 1, M1). The upper boundary condition for the flow system is a steady-state water table configuration (h_{wt}) (Dirichlet type) which was defined based on tomographic potentiometric (fluid potential) maps obtained from observation data (Máld-Szőnyi et al., 2019; Mádl-Szőnyi, 2019). In order to validate the numerical results, the calculated recharge rate (R) was compared to the estimated annual recharge (R') defined by Sehgal (1973) in inch/yr,

$$R' = 2.5\sqrt{P - 0.6} \quad (4)$$

where $P = 21.6$ inch/yr (550 mm/yr) denotes the annual precipitation (Mersich et al., 2003). It results in the maximum value of the annual recharge, $R' = 11.47$ inch/yr $= 291$ mm/yr which was used as an upper limit during the simulations. In this study, the recharge rate was calculated along the top of the numerical model given by

$$R = \frac{\int q_z(q_z < 0)dx}{\int (q_z < 0)dx} \quad (5)$$

where q_z denotes the vertical Darcy flux. The line integration was carried out on the recharge area of the model surface, where the vertical component of the Darcy flux points downward (q_z<0). In the base model (M1), the boundary conditions for flow were no-flow on the sides and bottom boundaries (Fig. 3a).

For the goals of the heat transport simulations, isothermal boundaries (M1) were described on the top ($T_s = 10\,^\circ$C) and along the bottom ($T_b = 225\,^\circ$C) in agreement with the average value of the geothermal gradient, $\nabla_z T = 45\,^\circ$C/km in the Buda Thermal Karst. In order to quantify the surface heat transfer, the results were compared to the conductive model by the non-dimensional Nusselt number (e.g. White, 1988),

$$Nu = \frac{q_{ths}}{q_{chs}} \quad (6)$$

where q_{ths} and q_{chs} are the total and the conductive heat flux on the surface, respectively. The side walls were assumed to be thermally insulated in the base model (M1).

The two-dimensional model was discretized by triangular and non-uniform finite elements (Fig. 3b), where the maximum element size was 100 m within the model domain, which was reduced to 20 m along the outer boundaries. The final mesh consisted of 201,799 finite elements. Within the elements, the solution was approximated by quadratic and linear functions for Darcy's Law (p) and the heat transport equation (T), respectively. Although in the conductive and forced thermal convection models, the numerical simulations produced steady-state solutions, the additional effect of thermal buoyancy resulted in transient groundwater flow and heat transport in the system (e.g. Kaiser et al., 2011; Havril et al., 2016; Przybycin, 2017; Havril, 2018; Szijártó et al., 2019). A total simulation time of 300 kyr was used to ensure that the system reached a quasi-stationary solution. At the beginning of the simulations (t<1 kyr), the maximum time-step increased exponentially, but thereafter remained constant at 100 yr. The time-dependent calculation for a given

Table 1
Physical parameters of the hydrostratigraphic units based on measured data and previous numerical simulations. Abbreviations: K, hydraulic conductivity; φ, porosity; ρ_{ma}, matrix density; λ_{ma}, thermal conductivity of matrix; c_{ma}, specific heat of matrix; Q_r, volumetric radioactive heat production. References: (1) Garamhegyi et al., 2020; (2) Rman and Tóth, 2011 (T-JAM project); (3) Tóth, 2018; (4) Máld-Szőnyi et al., 2019; (5) Eppelbaum et al., 2014; (6) Bodri, 1981; (7) Dövényi and Horváth, 1988; (8) Békési et al., 2018.

Hydrostratigrapic units	K (m/s)	Ref	φ (-)	Ref	ρ_{ma} (kg/m^3)	Ref	λ_{ma} (W/(m·K))	Ref	c_{ma} (kJ/(kg·K))	Ref	Q_r (μW/m^3)	Ref
HS1	10^{-6}	1	0.15	2	2200	5	1.8	6	0.84	5	1.2	7
HS2	$3\cdot10^{-7}$	1	0.10	2	2200	5	1.8	6	0.84	5	1.3	7
HS3	10^{-6}	3	0.10	2	2600	5	2.0	7	0.90	5	1.0	8
HS4	10^{-7}	4	0.10	4	2500	5	1.8	7	0.90	5	1.3	8
HS5	$3\cdot10^{-8}$	4	0.10	2	2500	5	1.8	7	0.90	5	1.5	8
HS6	10^{-8}	4	0.05	4	2000	5	1.5	7	2.10	5	1.6	8
HS7	10^{-6}	4	0.15	2	2100	5	2.0	7	0.84	5	1.5	8
HS8	10^{-5}	3	0.15	3	2700	5	2.5	6	0.85	5	0.5	8
HS9	10^{-5}	4	0.15	4	2750	5	2.6	7	0.85	5	0.5	8
HS10	10^{-5}	3	0.10	3	2700	5	2.2	5	0.80	5	0.5	8
HS11	10^{-7}	3	0.10	3	2750	5	2.2	5	0.80	5	0.5	8

Table 2
Model constants.

Definition	Symbol	Value	Units
Surface temperature	T_s	10	°C
Bottom temperature	T_b	225	°C
Thermal conductivity of water	λ_w	0.6	W/(m·K)
Specific heat of water	c_w	4.2	kJ/(kg·K)
Gravitational acceleration	g	9.81	m/s^2

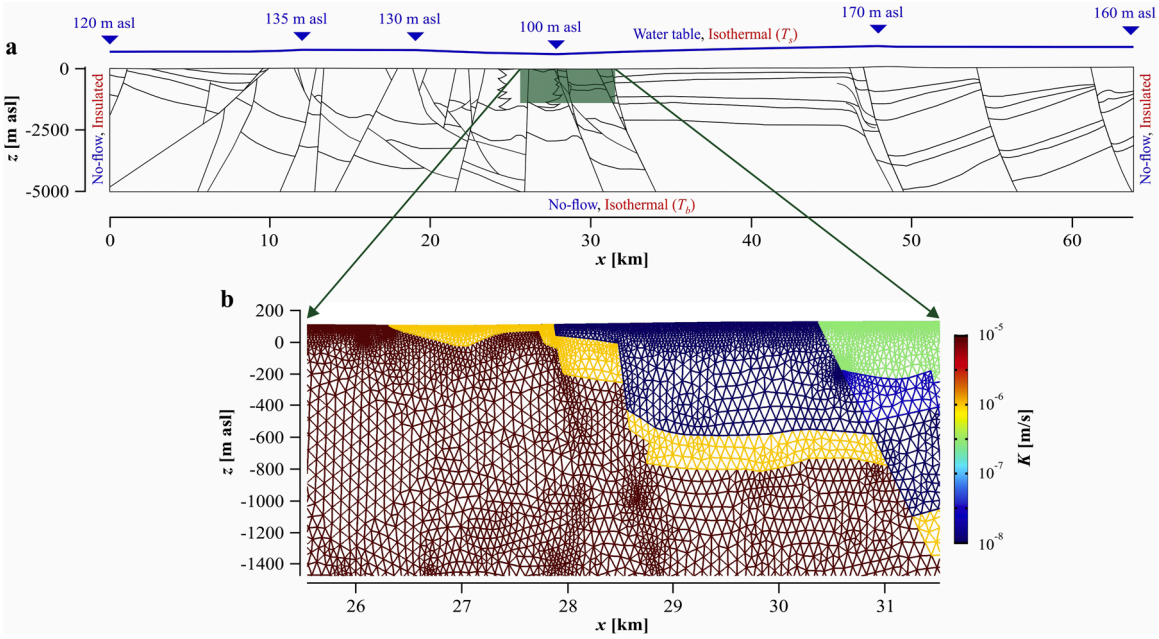

Fig. 3. (a) Model geometry with boundary conditions of Model 1. The water table configuration and the isothermal surface, as the upper boundary condition for the flow system (blue) and the heat transfer system (red), respectively. The vertical exaggeration is 1.5. (b) Illustration of the finite element discretization with the hydraulic conductivity of the HS2, HS5, HS6, HS7 and HS8 hydrostratigraphic units.

model required approx. 1–14 days CPU time and 10–20 GB memory on an Intel 2.79 GHz processor-based workstation with 24 cores.

3.2. Base simulation scenarios

Three main types of physical phenomena were examined to investigate the interaction of different driving forces in the BTK, Hungary. First, only conductive heat transport (Simulation 1, S1) was studied in order to quantify the additional effects of advection and thermal buoyancy in the transport processes. Second, the combined effect of topography-driven groundwater flow and advective heat transport (Simulation 2, S2) was investigated (forced thermal convection) (e.g. Clauser and Villinger, 1990; Mádl-Szőnyi and Tóth, 2015; An et al., 2015; etc.). In the third run, mixed thermal convection (Simulation 3, S3) caused by the interaction of forced and free thermal convection was simulated (e.g. Kaiser et al., 2013; Havril et al., 2016; Lopez et al., 2016; Havril, 2018; etc.), where Eqs. (1)–(3) were fully coupled by the Darcy flux (**q**) and the water density ($\rho_w(T,p)$). In this case, the initial condition for the pressure was generated by the steady-state solution of the purely topography-driven groundwater flow equations (Eqs. (1) and (2) with constant

Table 3
Models applied for the three basic simulation scenarios (Simulation 1–3).

Simulation 1–3	Flow boundary conditions		Thermal boundary conditions		Supplementary effect
Models	Bottom	Sides	Bottom	Sides	–
Model 1	No-flow	No-flow	Isothermal	Insulated	–
Model 2	No-flow	No-flow	Isothermal	Insulated	Conductive faults
Model 3	No-flow	No-flow	Isothermal	Insulated	Radiogenic heat production
Model 4a	No-flow	No-flow	Constant heat flux	Insulated	–
Model 4b	No-flow	No-flow	'Internal'	Insulated	–
Model 4c	No-flow	Hydrostatic pressure	Isothermal	Conductive temperature	–

water density), while the initial temperature distribution was defined by the solution of the conductive heat transport equation (Eq. (3) without heat advection). By the same token, the artificial effects of the pre-defined boundary conditions, as well as the influence of hydraulically conductive faults and radiogenic heat production, as natural effects, were also tested in the numerical models.

3.3. Further model scenarios

In addition to the investigation of the combined effect of driving forces, further numerical calculations were carried out to reveal the importance of natural (M2, M3) and artificial effects (M4a–4c) on regional groundwater flow patterns and temperature distribution in the numerical model. These results were separately compared to the base model (M1). Eventually, six models (M1–4c) were investigated in the cases of heat conduction (S1), forced (S2) and mixed thermal convection (S3) (Table 3). Thus, a total of 18 simulations were carried out.

3.3.1. Hydraulically conductive faults

In addition to the equivalent porous media (EPM) approximation, several methods have been established to study groundwater flow in fractured and karstified media, including deterministic numerical models and some stochastic methods for developing fracture or pipe networks (e.g. Berre et al., 2019). Applying the hybrid conception (Berre et al., 2019), Darcy's Law and the heat transport equation were also solved within the conductive faults (Fig. 2c),

$$\mathbf{q} = -\frac{K_f}{\rho_w g}\left[\nabla_t p - \rho_w \, g \, \nabla z\right] \tag{7}$$

$$\left[\varphi_f \rho_w c_w + \left(1-\varphi_f\right)\rho_f c_f\right]\frac{\partial T}{\partial t} + \rho_w c_w \mathbf{q}\nabla_t T = \nabla_t\left\{\left[\varphi_f \lambda_w + \left(1-\varphi_f\right)\lambda_f\right]\nabla_t T\right\} \tag{8}$$

where ∇_t denotes the tangential derivation, and the parameters characterizing the faults are listed in Table 4. We assume that the hydraulic conductivity of the faults was higher, by one order of magnitude, than in the surrounding medium (M2). Therefore, two different values were prescribed in the unconfined ($K_f^{UC} = 10^{-4}$ m/s) and the confined ($K_f^{C} = 10^{-7}$ m/s) part of the BTK.

3.3.2. Radiogenic heat production

The influence of radiogenic heat production was also considered in the numerical simulation (M3). The values of radioactive heat production established for the Cenozoic ($Q_r = 1.0$–1.5 μW/m^3) (HS1–HS7) and the Mesozoic ($Q_r = 0.5$ μW/m^3) layers (HS8–HS11) (Fig. 2) (Dövényi and Horváth, 1988; Békési et al., 2018) were integrated into the numerical model (Table 1).

3.3.3. Boundary conditions

As bottom thermal boundary conditions, either constant temperature (T_b) or heat flux (q_{hb}) are usually applied in numerical calculations. In order to investigate the effects of the bottom thermal boundary on basin-scale heat transport processes, two other scenarios were studied: a constant bottom heat flux, $q_{hb} = 100$ mW/m^2 (M4a) and an 'internal' condition (M4b). In the latter model, an extra layer with a thickness of 2 km is set beneath the original model as a basement (Paleozoic metamorphic rock) (Table 5). In this model, the temperature of the isothermal bottom boundary was T_b(z=-7000 masl) = 315 °C. The artificial influence of the side walls was also investigated using two scenarios: a no-flow – insulated (M1) and a hydrostatic pressure – conductive temperature (M4c) boundary condition (Table 3).

4. Results and interpretation

First, results from the numerical solution of the base model (S1–3, M1) are presented to highlight the role of the governing transport mechanisms of heat conduction, forced and mixed thermal convection in the Buda Thermal Karst (BTK). Second, the effects of the hydraulically conductive faults (M2) and radioactive heat production (M3) on the temperature field and groundwater flow pattern are investigated. Finally, the influence of artificial boundary conditions is studied (M4a–4c).

Table 4
Model parameters of the conductive faults on the unconfined (west) and the confined (east) side of the numerical model (Model 2, M2).

Definition	Symbol	Value	Units
Hydraulic conductivity on the (west) unconfined side of the BTK	$K_f{}^{UC}$	10^{-4}	m/s
Hydraulic conductivity on the (east) confined side of the BTK	$K_f{}^{C}$	10^{-7}	m/s
Porosity	φ_f	0.1	–
Density	ρ_f	2500	kg/m^3
Thermal conductivity of matrix	λ_f	2	W/(m·K)
Specific heat of matrix	c_f	0.85	kJ/(kg·K)
Characteristic thickness	d_f	5	m

Table 5
Model parameters of the lower, impervious domain in Model 4b (M4b).

Definition	Symbol	Value	Units
Hydraulic conductivity	K_i	10^{-10}	m/s
Porosity	φ_i	0.01	–
Density	ρ_i	2800	kg/m^3
Thermal conductivity of matrix	λ_i	2.4	W/(m·K)
Specific heat of matrix	c_i	0.8	kJ/(kg·K)

4.1. Thermal conduction

The pure conductive heat transport mechanism was first investigated in the two-dimensional numerical model (Fig. 4). In this simplest case, heat flow is disturbed neither by advective heat transport due to water table variations, nor by thermal buoyancy due to water density variation. Regarding the minor difference in thermal conductivities of the hydrostratigraphic units (λ_{ma}=1.8–2.6 W/(m·K)), the simulated vertical temperature profile closely follows a linear distribution. In the base model (S1, M1), the average value of the total surface heat flux is $q_{chs} = 80.86$ mW/m^2, which is used as a standard for calculating the non-dimensional Nusselt number (Eq. (6)).

4.2. Forced thermal convection

In the base model, the influence of forced thermal convection (S2, M1), which includes the superposition of the advective and the conductive heat transfer mechanisms, on the temperature distribution, is displayed in Fig. 5a. Because of the isothermal boundary condition on the top of the model, water enters the system at the temperature of $T_s = 10$ °C in the areas with high water table elevation. One of the most significant cooling effects is found beneath the unconfined karstified carbonate ($x = 8$–26 km), where the cold water can directly infiltrate to 3 and 4 km deep and towards the discharge areas. This effect is owing to the high hydraulic conductivity of the Triassic aquifers (HS8, HS9, HS10) and the high hydraulic gradient due to water table configuration ($h = 130$ masl). On the eastern side of the model ($x = 47$–63.8 km), the temperature distribution is also influenced by advective cooling due to the topography-driven groundwater flow and the deep position of the low permeability hydrostratigraphic unit (HS6). On the other hand, a positive temperature anomaly evolves in the main discharge area near the Danube River ($x = 26$–28 km), where the thermal water approaches the top of the model at a temperature of $T = 70$–80 °C. The conductive temperature field is less perturbed between $x = 0$ and 8 km, as well as between $x = 33$ and 47 km where the intensity of the topography-driven groundwater flow decreases with depth (Fig. 5b).

In the steady-state numerical model, the magnitude of the Darcy flux (q) varies within a range of 10^{-12} and 10^{-6} m/s (Fig. 5b). Due to the elevated fluid potential and the high hydraulic conductivity of the Triassic aquifers (HS8, HS9, HS10), the Darcy flux in this area exceeds 10^{-9} m/s. The fluid potential maximum in the siliciclastic Gödöllő Hills induces intensive local groundwater flow in the upper part of the model ($x = 48$–51 km). However, the intensity of the groundwater flow is two orders of magnitude lower in the confining sedimentary cover (HS1, HS2, HS5, HS6, HS7) and in the Lower-Triassic and Paleozoic aquitard (HS11) compared to the Triassic aquifers (Figs. 2c and 5 b).

In the case of forced thermal convection (S2), the hydraulic head distribution was calculated from the simulated pressure, p, according to the following formula:

$$h_{FC} = \frac{p}{\rho_w(T_s = 10^\circ\,\mathrm{C}, p)g} + z, \tag{9}$$

using the pressure-dependent water density at the surface temperature of $T_s = 10$ °C. Fig. 5c illustrates the hydraulic head distribution within a range of $h_{FC} = 100$ masl and 170 masl. The groundwater flow pattern is characterized by streamlines, moreover recharge (R) or discharge (D) zones are indicated with red and blue colors, respectively. (Non-uniform and not magnitude controlled streamlines were used to visualize the groundwater direction in the entire model domain.) As a result of this steady-state simulation, three main groundwater systems evolve in the numerical model with two directions denoted by magenta (from east to west) and yellow (from west

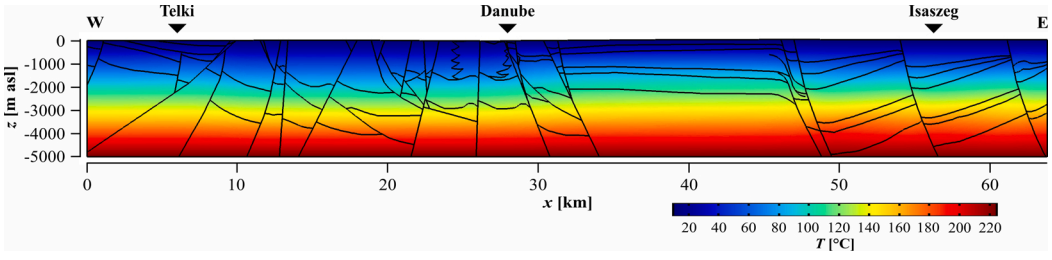

Fig. 4. Conductive temperature distribution in the base model (S1, M1). The vertical exaggeration is 1.5. Telki, Danube and Isaszeg denote the locations of the vertical temperature profiles.

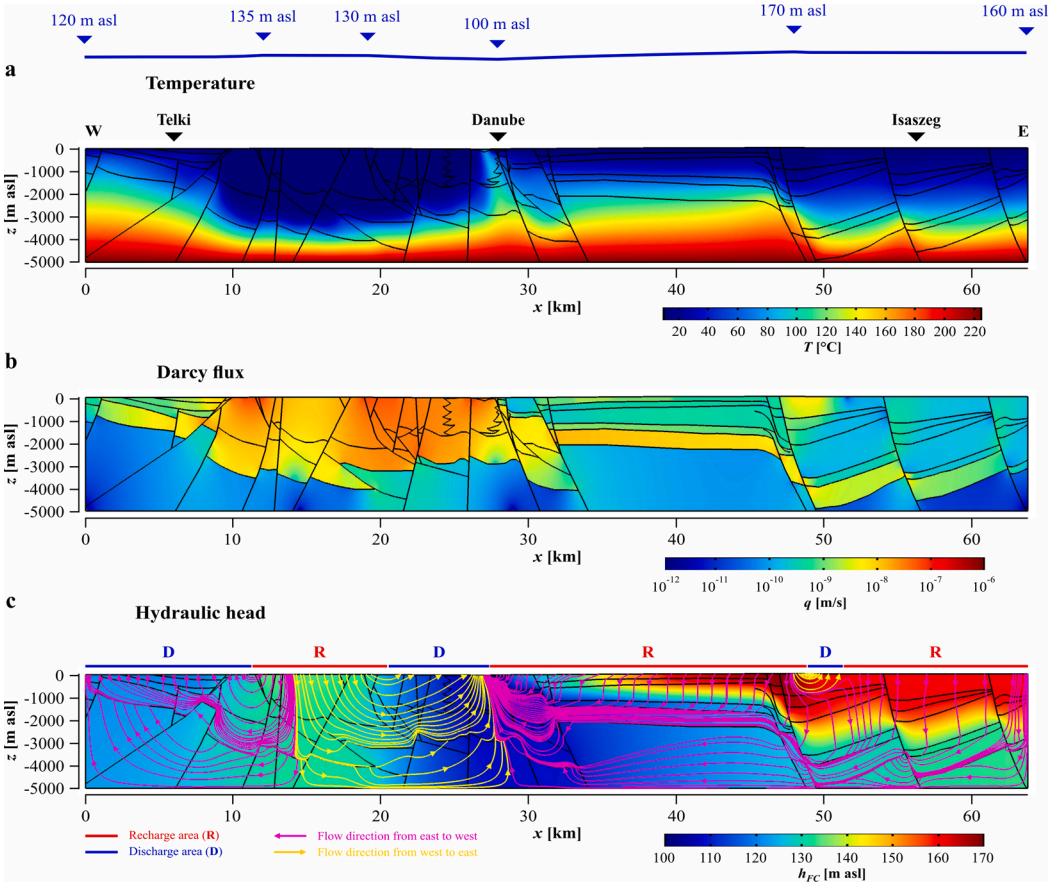

Fig. 5. Steady-state solution of (a) temperature, (b) Darcy flux and (c) hydraulic head due to forced thermal convection in the base model (S2, M1). The water table configuration, as the upper boundary condition for the flow, is indicated by the blue line. The magenta and the yellow streamlines represent the flow direction from east to west and from west to east, respectively. The streamlines are non-uniform and not magnitude controlled to visualize the groundwater flow direction in the entire model domain. The recharge and discharge areas are denoted with different colors. Telki, Danube and Isaszeg denote the locations of the vertical temperature profiles.

to east). On the western side, a recharge area is noted from $x = 11$ km–20.5 km, where the cold water can infiltrate into the deeper parts due to the unconfined Triassic carbonate with high hydraulic conductivity (HS8, HS9, HS10) (Fig. 2c). From this recharge area, two groundwater flow systems evolve which are separated by a divergent stagnation zone at $x = 14$ km and at a depth of 5 km (Fig. 5b, c). The entire eastern side of the model is identified as a recharge area, where the surface water infiltrates moderately, except for a valley in the Gödöllő Hills ($x = 50$ km), where a relatively more intense local groundwater flow system forms. Beneath the main discharge area, near the Danube River, the two groundwater flow systems originating from the west and the east are mixing through the total depth of the model (Fig. 5c). This indicates a convergent stagnation point. These stagnation zones are consequences of the bottom boundary condition, and they are revealed in Fig. 5b, where the Darcy flux decreases below $q = 10^{-11}$ m/s. As a result of the advective heat transport mechanism, the non-dimensional Nusselt number increased to $Nu = 1.66$ (i.e. the total surface heat flux increased by 66 % compared to conductive heat flow), and the calculated average recharge rate was $R = 157$ mm/yr in the base model (S2, M1).

4.3. Mixed thermal convection

In the third case, the combined effect of the three transport mechanisms was studied in the base model (S3, M1). Heat conduction, topography-driven forced thermal convection and buoyancy-driven free thermal convection were investigated as a fully-coupled physical problem. Over the entire model domain, the non-dimensional Rayleigh number (e.g. Nield and Bejan, 2017) exceeds its critical value ($Ra = 4700 >> Ra_{cr} = 4\pi^2$), while the modified Péclet number (Szijártó et al., 2019) reaches $Pe^* = 42.5$. At these values, time-dependent mixed thermal convection is expected based on former theoretical model calculations (Szijártó et al., 2019), which underlines the importance of thermal buoyancy forces in the BTK system.

The influence of mixed thermal convection is displayed on the temperature distribution in Fig. 6, which shows temperature snapshots from $t = 100$–300 kyr. As a result of mixed thermal convection, a time-dependent flow system forms in the base model (S3, M1). The change in temperature field (Fig. 6a–e) indicates non-stationary flow. On the unconfined side, significant advective cooling

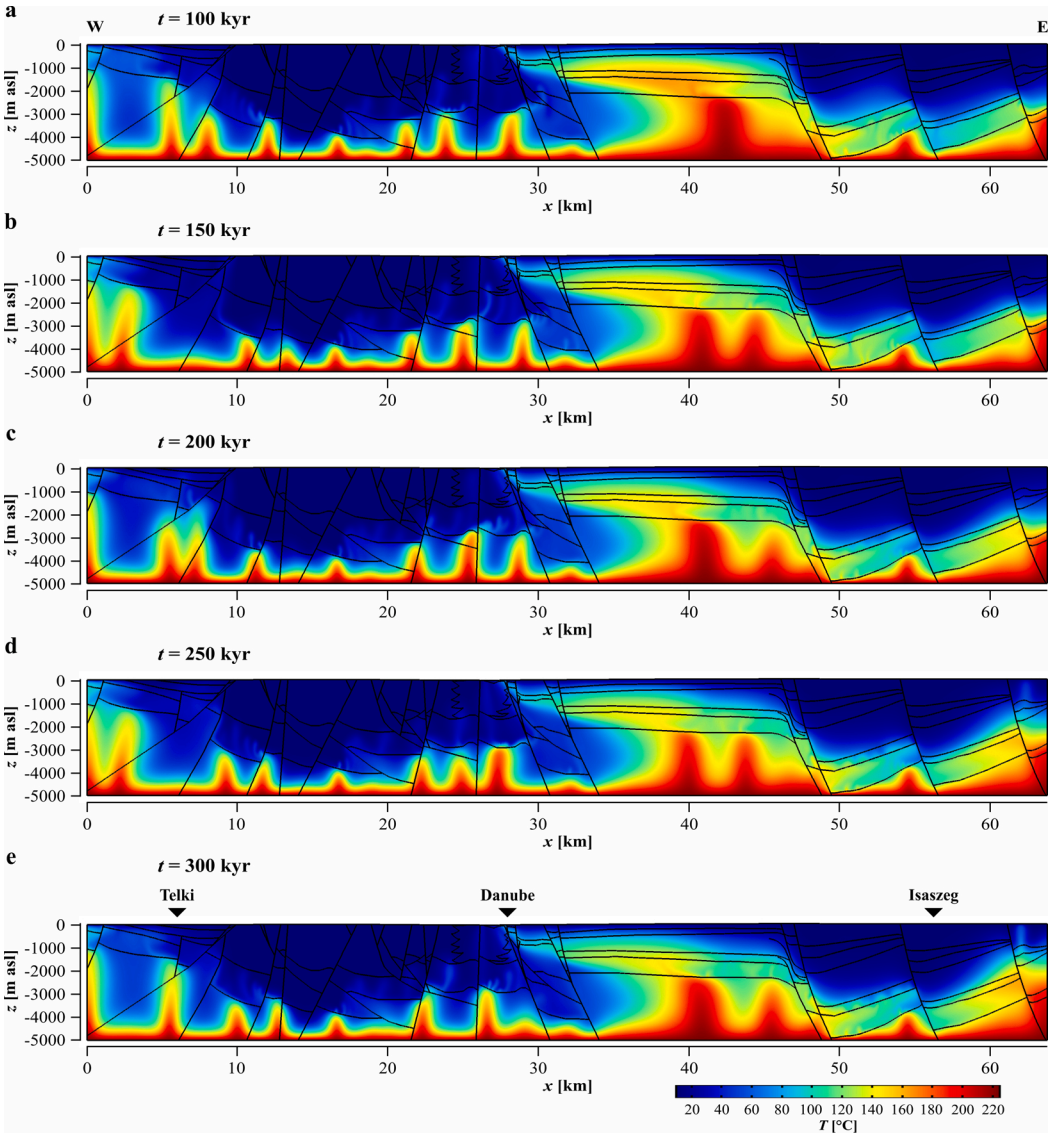

Fig. 6. Temperature snapshots at times of (a) $t = 100$ kyr, (b) $t = 150$ kyr, (c) $t = 200$ kyr, (d) $t = 250$ kyr and (e) $t = 300$ kyr, representing the temperature field of the mixed thermal convection (S3; M1). Telki, Danube and Isaszeg denote the locations of the vertical temperature profiles.

can be noticed within the range of $x = 7$ km and 27 km in the Triassic carbonates (HS8, HS9, HS10 in Fig. 2c), which overlaps with the results from the forced thermal convection model (Fig. 5a). However, weaker plumes evolve from the bottom of the unconfined (western) side of the model which are swept towards the discharge area beneath the Danube River. Thermal buoyancy is thus superimposed on forced thermal convection. These plumes are able to reach the near-surface region at the discharge area within a temperature range of $T = 40$–60 °C. Under the siliciclastic covers of the eastern side, further convection cells develop in the Triassic aquifer (HS8). Because of the lower hydraulic conductivities of the Triassic-Paleozoic aquitard (HS11), and the sedimentary covers (HS2, HS5, HS6, HS7), a large hot upwelling forms beneath the Pest Plain ($x = 33$–48 km), where the thermal water ($T = 100$–120 °C) moves directly toward the main discharge zone at the Danube River. This hot upwelling upheld by forced thermal convection remains in a stable position. An animation in Appendix B presents the time-dependent behavior of the temperature field in mixed thermal convection system from $t = 150$–300 kyr

The distributions of the Darcy flux and the hydraulic head with streamlines are illustrated in Fig. 7 at time $t = 300$ kyr (parallel to Fig. 6e). The increased Darcy flux shows the position of the hot plumes in the deeper part of the numerical model, and in the hydrostratigraphic units with high hydraulic conductivities (HS8 and HS7) (Fig. 7a). In the middle part of the model, the location of groundwater flow mixing shifted east to $x = 41$ km (Figs. 6e and 7 b) compared to the forced thermal convection model $x = 28$ km (Figs. 5a and 5 c). The flow directions indicated by yellow display the penetration of recharging water from Buda under the Pest side.

Time-dependent stagnation zones ($q < 10^{-11}$ m/s) evolve between the depths of 4.5 and 5 km. The hydraulic head was calculated for

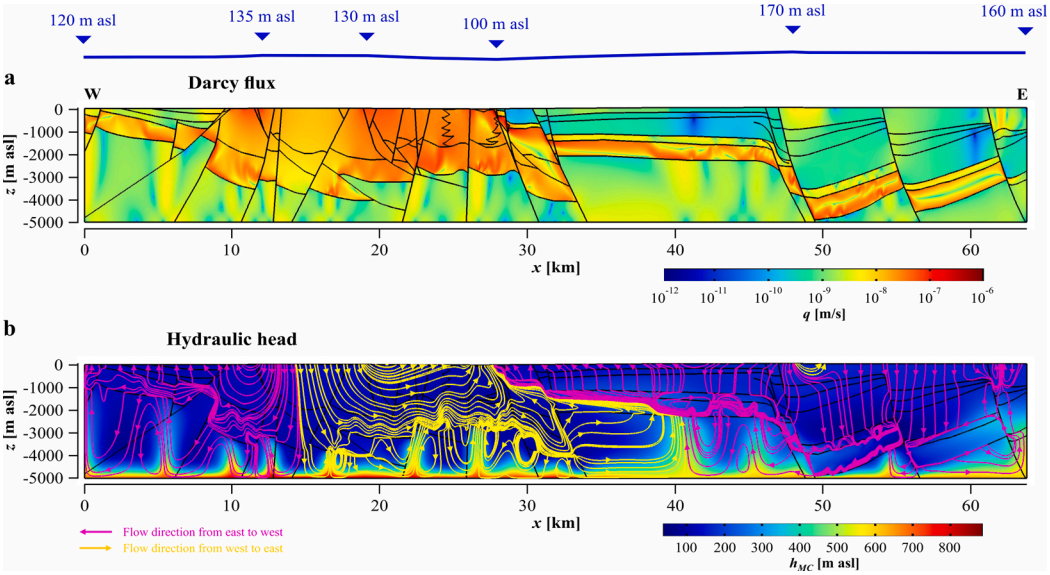

Fig. 7. Snapshots of (a) the Darcy flux and (b) the hydraulic head in the mixed thermal convection base model (S3, M1) at a time of $t = 300$ kyr. The Darcy flux direction is illustrated by streamlines as in Fig. 5c. The streamlines are non-uniform and not magnitude controlled to visualize the groundwater flow direction in the entire model domain. The water table configuration, as the upper boundary condition for the flow, is indicated by the blue line.

the fully-coupled mixed thermal convection model (S3) using the temperature- and pressure-dependent water density,

$$h_{MC} = \frac{p}{\rho_w(T,p)g} + z \tag{10}$$

The high anomalies in hydraulic heads (h_{MC}>400 masl) are the consequences of the significant density decrease in the thermal boundary layer and in the stable large hot upwellings (Fig. 7b). We note that h_{MC} includes the temperature dependence of water density, while h_{FC} in Eq. (9) is calculated from constant temperature ($T_s = 10$ °C).

The analyses of the time series for different models (S3) are shown over a time interval of $t = 0$–300 kyr in Fig. 8, where the base model (M1) is illustrated by a black line. After the transient behavior of the system (t>150 kyr), when the initial conductive temperature field was strongly modified by the mixed heat transfer mechanism, the monitoring parameters tended to a quasi-stationary solution with a characteristic time period of approx. $\tau = 10$–100 kyr (Fig. 8). As a result of the additional free thermal convection (S3, M1), the non-dimensional Nusselt number (Nu) varied between 3.5 and 5.5, while the calculated recharge rate (R) was within a range of $R = 235$ mm/yr and 265 mm/yr. In Appendix A (Supplementary data), the time-dependence of the temperature field and hydraulic head distribution is illustrated at 8 near-surface probe points. As a result, a longer ($\tau_I \approx 40$–50 kyr) and a shorter characteristic time scale ($\tau_{II} \approx 1$–2 kyr) were noticed from the examined temperature and hydraulic head time series. The animation of the temperature field can improve the understanding of the characteristic behavior of mixed thermal convection (Appendix B – Supplementary data).

The results for Model 1 in Fig. 9 show the time-averaged value of the Nusselt number and the recharge rate in the cases of pure heat

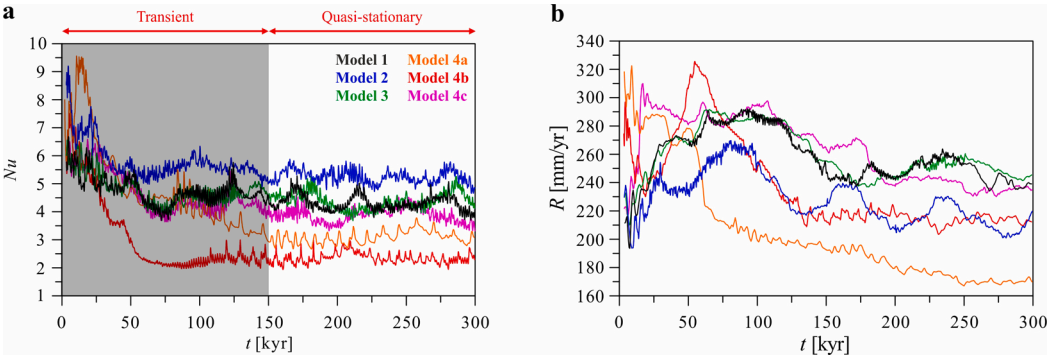

Fig. 8. Time series showing (a) the non-dimensional Nusselt number (Nu) and (b) the recharge rate (R) in the different numerical models (S3, M1–M4c). Time-averaged values are calculated for the quasi-stationary time interval (t>150 kyr). The model scenarios (Table 3) are illustrated by different colors.

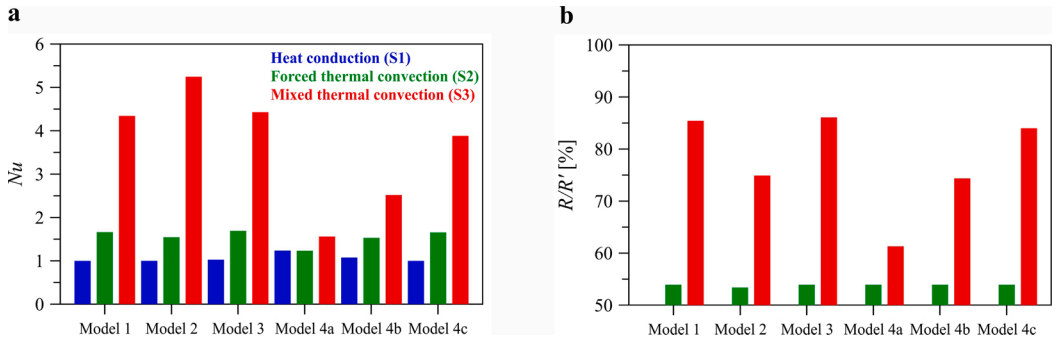

Fig. 9. Time-averaged values of the time series of (a) the Nusselt number (*Nu*) and (b) the normalized recharge rate (*R/R'*) over the quasi-stationary time interval in the cases of pure conduction (S1, blue), forced thermal convection (S2, green) and mixed thermal convection (S3, red). The model scenarios are listed in Table 3. In the pure heat conduction simulations (blue), there is no groundwater flow, so the normalized recharge rate cannot be calculated in Fig. 9b.

conduction (blue, S1), forced (green, S2), and mixed thermal convection (red, S3). The recharge rate was normalized by the estimated annual recharge (*R/R'*). In the base model (S3, M1), the intensive hot upwellings induced an enhanced heat flux on the surface. Thus, the Nusselt number was almost three times greater than that under forced thermal convection ($Nu = 1.66$). In the cases of forced (S2, M1) and mixed thermal convection (S3, M1), the normalized recharge rates (*R/R'*) were 54% and 85%, respectively (Fig. 9b).

Based on these numerical results, the existence of free thermal convection can be expected in the Buda Thermal Karst due to the high geothermal gradient and hydraulic conductivity of the Triassic aquifers (HS8, HS9, HS10), and the reduced water table slope (Fig. 2). Time-dependent mixed thermal convection developed in the base model (S3, M1) (Fig. 8), where hot plumes were continuously evolving from the thermal boundary layer, ascend and are swept towards the regional discharge area (Fig. 6e).

4.4. Further model scenarios

4.4.1. Effects of hydraulically conductive faults

In the heterogeneous base model (M1), an equivalent porous media (EPM) approximation was applied in the homogeneous, isotropic hydrostratigraphic units (Table 1). This model was modified to a hybrid model (M2) in order to investigate the effect of hydraulically conductive faults on the groundwater flow system (Fig. 2c). Because of the large difference between the characteristic length scale of the flow system ($L/2 \approx 32$ km) and the thickness of the conductive faults ($d_f = 5$ m), this modification does not induce notable changes in the temperature (Fig. 10a) and the Darcy flux distribution (Fig. 11a) compared to the base model (S3, M1) (Figs. 6e and 7 a). In the case of forced thermal convection (S2, M2), the non-dimensional Nusselt number decreased by 7% (Fig. 9). With mixed thermal convection, the non-dimensional Nusselt number increased by 21%, while the normalized recharge rate decreased by 10%, compared to the base model (S3, M1). The movement of hot upwellings is facilitated by hydraulically (and thus thermally) conductive faults towards the near-surface zone, which can locally influence the extent of the recharge and the discharge areas. Consequently, the conductive faults are also able to influence the heat flux and the recharge rate (Fig. 9), but this impact seems insignificant on the regional-scale temperature and Darcy flux fields (Figs. 10a and 11 a).

4.4.2. Effects of radiogenic heat production

An additional numerical model scenario was developed to investigate the effect of radiogenic heat production (Table 1). In the heat conduction model, the surface heat flux increases by only 2 mW/m^2 due to this added heat production mechanism (S1, M3). In the forced thermal convection model (S2, M3), neither the Nusselt number nor the recharge rate are disturbed by the additional effect of radiogenic heat compared to the base model (Fig. 9). Apparent variations due to buoyancy forces cannot be noticed qualitatively in the temperature and the Darcy flux in Figs. 10b and 11 b, respectively (S3, M3). The changes in the time-averaged value of the Nusselt number and the normalized recharge rate remains below 2% (Fig. 9), which is also shown by the time series in Fig. 8. In general, the additional effect of the radiogenic heat production is negligible.

4.4.3. Effects of boundary conditions

In this part, differences in the numerical results due to the boundary conditions are investigated, compared to the base model having an isothermal bottom boundary, $T_b = 225$ °C. In Model 4a, a constant heat flux of $q_{hb} = 100$ mW/m^2 was prescribed along the bottom boundary. In the cases of heat conduction (S1, M4a) and forced thermal convection (S2, M4a), the non-dimensional Nusselt number increased by 24% compared to the conductive base model (S1, M1) (Fig. 9) owing to the ratio of bottom heat fluxes, $q_{hb}/q_{chs} = 100/80.86 = 1.237$. Focusing on the mixed convection simulations, the discrepancy between Model 1 (Fig. 6e) and Model 4a (Fig. 10c) is the lack of the bottom thermal boundary layer, thus the temperature significantly decreases in the Triassic and Lower-Paleozoic aquitard (HS11). Although the additional effect of free thermal convection weakens, the main hot upwellings stay in stable positions in the deeper parts of the model domain. The change in the bottom thermal boundary condition resulted in 64% and 28% drops in the Nusselt number and the recharge rate, respectively, due to the less intensive heat transport in Model 4a (S3, M4a).

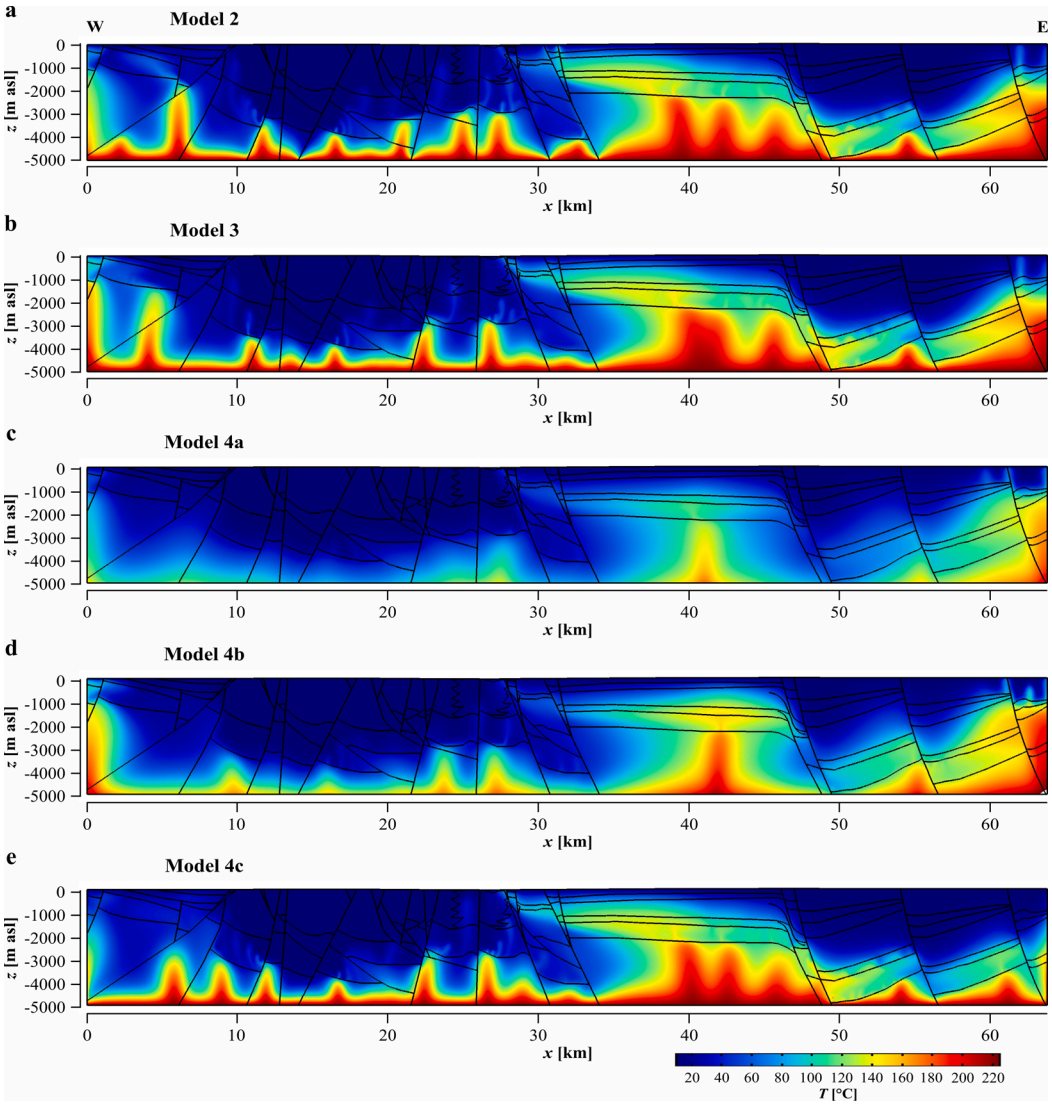

Fig. 10. Snapshots of the temperature at a time of $t = 300$ kyr at different model scenarios (Table 3) representing the effect of natural phenomena: (a) hydraulically conductive faults (M2), (b) radiogenic heat production (M3); and representing the effect of boundary conditions: (c) constant bottom heat flux (M4a), (d) 'internal' thermal boundary condition on the bottom (M4b) and (e) modified boundary conditions on the side walls (M4c) in the case of mixed thermal convection.

In addition, an 'internal' thermal boundary condition was tested by a lower, quasi-impermeable domain with a thickness of 2 km in order to reveal the influence of assuming that neither the temperature nor the heat flux is constant at a depth of 5 km. Although a strong thermal boundary layer is not formed along the bottom of Model 4b (Fig. 10d), the thermal anomalies become stronger in the deeper regions compared to Model 4a (Fig. 10c). This 'internal' thermal boundary condition is therefore between the two types of conventionally applied boundary conditions, constant temperature (Fig. 6e) and constant heat flux (Fig. 10c). Compared to the base model (S3, M1), the Nusselt number is reduced by 8% and 42% in the advective (S2, M4b) and in the fully coupled (S3, M4b) heat transfer simulations, respectively (Fig. 9a). Furthermore, the normalized recharge rate (R/R') decreased by 11%, permitting free thermal convection (S3, M4b) (Fig. 9b).

Finally, the influence of the side walls as a no-flow – thermally insulated (Fig. 6e) versus a hydrostatic pressure – conductive temperature boundary condition (Fig. 10e) was investigated (Table 3). These conditions are consistent with the initial thermal and flow fields. In the case of mixed thermal convection (S3, M1), the no-flow – thermally insulated boundary condition stabilizes the flow and the temperature field near the walls, so upwelling hot plumes are facilitated (Fig. 6e). However, the hydrostatic pressure – conductive temperature condition (S3, M4c) allows groundwater flow through the side walls (Figs. 10e and 11 e). Thus, the vertical boundary conditions of Model 4c do not favor any upwellings along the side walls (Fig. 10e) in contrast to Model 1 (Figs. 6e and 7 a). In this case, the applied boundary conditions influence the temperature and Darcy flux distribution in the vicinity (approx. 5 km) of the

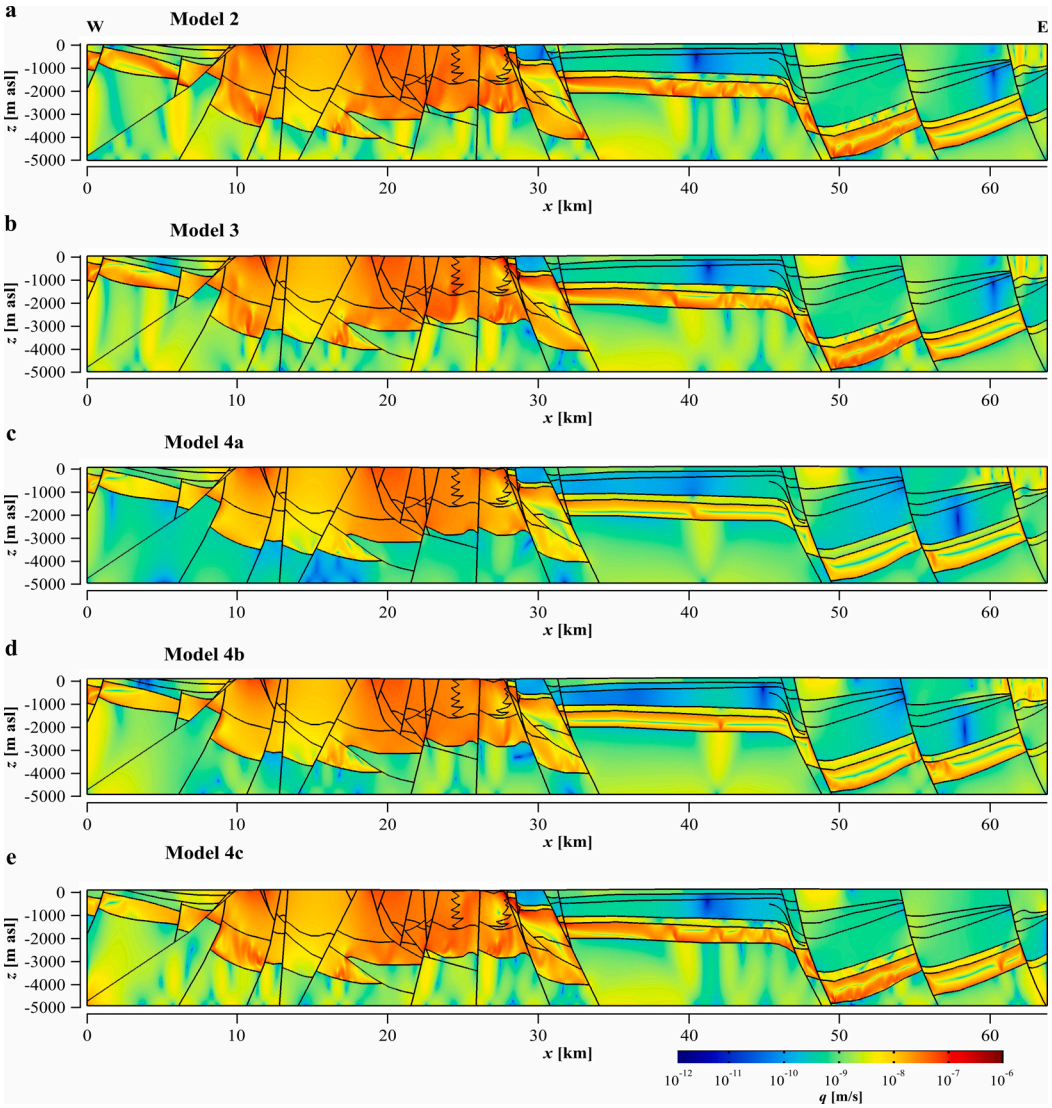

Fig. 11. Snapshots of the Darcy flux at a time of $t = 300$ kyr at different model scenarios (Table 3) representing the effect of natural phenomena: (a) hydraulically conductive faults (M2), (b) radiogenic heat production (M3); and representing the effect of boundary conditions: (c) constant bottom heat flux (M4a), (d) 'internal' thermal boundary condition on the bottom (M4b) and (e) modified boundary conditions on the side walls (M4c) in the case of mixed thermal convection.

side walls. The time series of *Nu* and *R* are illustrated in Fig. 8 by magenta curves, which do not significantly deviate from the base model (black). In this scenario (S3, M4c), the time-averaged value of the Nusselt number decreased by 11%, while the normalized recharge rate decreased by 1.5% compared to the base model (S3, M1) (Fig. 9). Consequently, the studied boundary conditions affect the flow and the temperature field near the side walls. Nevertheless, independently of the investigated boundary conditions along the bottom and the side walls, time-dependent mixed thermal convection evolved in each numerical model.

5. Discussion

In this study a finite element numerical method was applied to understand the basin-scale flow system and temperature distribution for an area with complex geology in cases of three coherent heat transport mechanisms which were (1) heat conduction (S1), (2) forced thermal convection (S2) (i.e. advective and conductive heat transport mechanisms) and (3) mixed thermal convection (S3) (i.e. conduction and advection with thermal buoyancy). Based on our numerical results presented above, the existence of free thermal convection superimposed on forced thermal convection cannot be excluded from the transport mechanism in the Buda Thermal Karst (BTK) system of Hungary.

Three vertical temperature $T(z)$ profiles were extracted from the base model (M1) and compared to well observation data. During

the application of the basin-scale data evaluation method (e.g. Tóth, 2009), three interpreted temperature profiles (Telki, Danube, Isaszeg) were presented by Máld-Szőnyi et al. (2019) and Mádl-Szőnyi (2019) in the different parts of the BTK. Figs. 4, 5a and 6 e show the position of the $T(z)$ profiles, where the centres of the interpreted areas were at $x = 6$ km (Telki), $x = 28$ km (Danube) and $x = 56$ km (Isaszeg). In Fig. 12, the simulated and measured temperatures are illustrated with the calculated geothermal gradients. (The reliable measured temperature data are above the elevation of z=−1500 masl, so the geothermal gradients from the numerical models ($\nabla_z T_N$) and from the observations ($\nabla_z T_M$) are presented only within this interval.) Profiles obtained from the conduction, forced and mixed thermal convection models (S1, S2, S3; M1) are denoted by blue, green and red colors, respectively.

First, the numerical results and the measured temperature data were compared beneath the Telki ($x = 6$ km) observation area (Fig. 12a, d, g). Although the geothermal gradient calculated by the measured data ($\nabla_z T_M = 39.4$ °C/km) is close to a conductive temperature profile ($\nabla_z T_{NC} = 46$ °C/km) (Fig. 12a), a discharge area was noticed in the cases of both forced (Fig. 5c) and mixed thermal convection (Fig. 7b). The purely advective heat transport cases (S2, M1) induce an increase in the geothermal gradient near the surface ($\nabla_z T_{NF1}(z > -140\ \text{masl}) = 66.9$ °C/km) and a decrease between the elevation of z=−140 masl and −970 masl

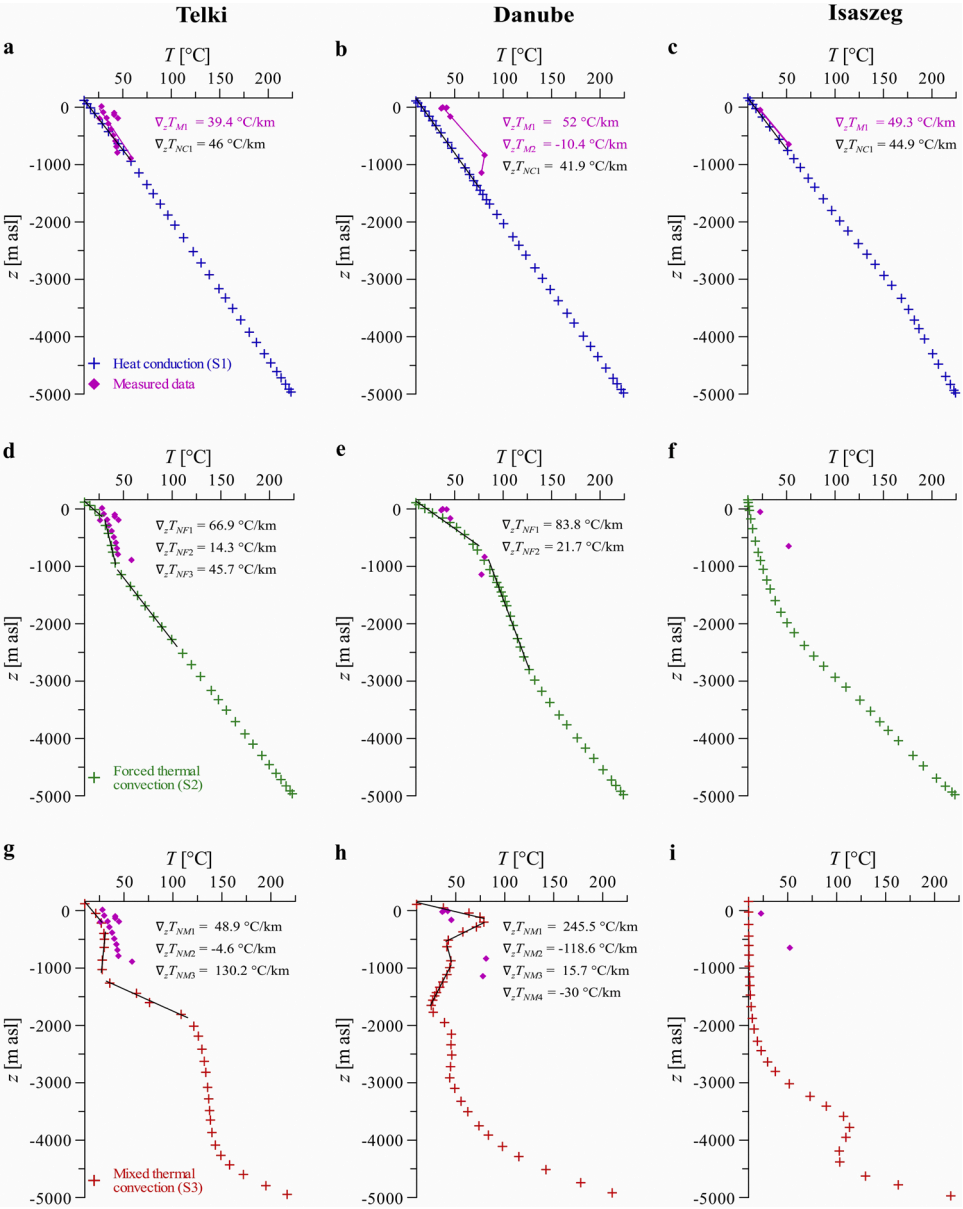

Fig. 12. Vertical temperature profiles in the cases of conduction (a, b, c), forced (d, e, f) and mixed thermal convection (g, h, i) denoted by blue, green and red colors, respectively. The locations of the $T(z)$ profiles (Telki, Danube, Isaszeg) along the hydrostratigraphic section are shown in Fig. 4, 5a and 6e. The temperature data from the numerical base model (S1–3; M1) at $t = 300$ kyr and from the observations (Máld-Szőnyi et al., 2019; Mádl-Szőnyi, 2019) are illustrated by crosses and diamonds, respectively.

($\nabla_z T_{NF2}(-140\,\text{masl}>z>-970\,\text{masl}) = 14.3\,^\circ\text{C/km}$) (Fig. 12d). Beneath the elevation of z=-1000 masl, the geothermal gradient changed to close to the conductive value. In the case of mixed thermal convection (S3, M1), the simulated geothermal gradients seem to be exaggerated compared to the observations (Fig. 12g).

Second, the temperature profiles were compared beneath the Danube River (Fig. 12b, e, h). The measured temperature data are much higher than the results from the conductive model simulation (S1, M1) (Fig. 12b), and the difference in the geothermal gradients reaches 10 °C/km near the surface. The geothermal gradient obtained from the advective numerical simulation (S2, M1) increased above the elevation of z=-640 masl due to topography-driven forced thermal convection (Fig. 12e). The forced convection case is also characterized by a steady-state hot upwelling beneath the regional discharge area (Fig. 5a). However, the negative geothermal gradient obtained from temperature observations between z=-830 masl and −1150 masl can be interpreted only by the existence of time-dependent free thermal convection (S3, M3) with inclined hot plumes (Fig. 12h). In this case, the location of the groundwater mixing zone was shifted toward the confined part by approx. 10–15 km (Fig. 7b). This model result coincides with previous studies in which the temperature and the geochemical properties of springs were analysed in the BTK (Mádl-Szőnyi and Tóth, 2015; Mádl-Szőnyi et al., 2018; Mádl-Szőnyi, 2019; Máld-Szőnyi et al., 2019; Erőss, 2010; Erőss et al., 2012; etc.).

Third, the temperatures from the numerical simulations and from the observations were compared beneath Isaszeg ($x = 56$ km, Fig. 12c, f and i) to examine the effect of heat transport processes in a typical recharge area. The numerical simulations showed a considerable cooling effect of advective heat transport (Figs. 5a and 6 e), which overwrote the initial conductive temperature distribution (Fig. 4). However, a noticeable correspondence between the simulated ($\nabla_z T_{NC1} = 44.9\,^\circ\text{C/km}$) and the measured ($\nabla_z T_{M1} = 49.3\,^\circ\text{C/km}$) geothermal gradients was found in the case of pure heat conduction (Fig. 12c). Therefore, a less intensive groundwater flow component can be established under the eastern, confined part of the Buda Thermal Karst system owing to, for instance, the higher hydraulic anisotropy of the Cenozoic layers.

Finally, a two-dimensional temperature field was calculated from the Geothermal Database of Hungary (Dövényi, 1994) along a section (Fig. 1c) to display the measured temperature data. The measured temperature data were projected using a space interval with a width of 10 km (Fig. 1c). A Gaussian regression interpolation method was applied on the temperature data with different locations and elevations (200 masl>z>−1500 masl) in order to set up a two-dimensional temperature section (Fig. 13). On the western side of the temperature section (x<10 km), a significant cooling effect due to advective heat transport is noted above the elevation of z=-750 masl. A large-scale heating effect of forced or mixed thermal convection was noted beneath the regional discharge area, the Danube River (24 km<x<33 km) (Fig. 13b). There, the negative temperature anomaly might also have evolved due to the time-dependent mixed thermal convection which was suggested by the numerical simulations. On the eastern side of the studied section (x>40 km), a shallow advective cooling effect is identified (z>-400 masl) which changes to a mainly conductive temperature field with depth due to the possible anisotropy of the Miocene aquifers (HS1 and HS2) (Garamhegyi et al., 2020).

In addition, a former study, which focused on changes in the temperature field and flow pattern using a simplified geology of the BTK from the Late Miocene to present day, revealed periodic temperature oscillations in the groundwater flow system within a range of 15 kyr and 40 kyr (Havril, 2018). According to a comprehensive field observation and description, and subsequent petrographic, mineralogic and isotopic analyses of speleothems in the caves of BTK, water level fluctuations and groundwater temperatures were reconstructed for the last 500 kyr (Virág, 2019). The position and different forms of calcite rafts, cave popcorns and cauliflower coatings revealed a water table rise of ~5–7 m in the period of ~300–280 kyr ago. Simultaneously, the carbonate precipitates indicated an increase in groundwater temperature from ~28 °C to ~48 °C. Then, a gradual decline of the water table (~10 m) and cooling of groundwater (~30 °C) were recorded by the speleothems in the following ~130 kyr. The time-dependent quasi-periodic behavior of mixed thermal convection might be one of the feasible explanations for the mentioned observations in the Buda Thermal Karst (Appendix A and B – Supplementary data).

6. Summary and conclusions

Finite element numerical simulations were performed to investigate the role of heat conduction, advection and thermal buoyancy, as physical mechanisms in the groundwater flow system and temperature distribution of the well-studied area of the Buda Thermal Karst of Hungary. In addition to three basic scenarios (S1–3, M1), five further models (M2–M4c) were tested to study the additional effects of natural phenomena and of the effects the boundary conditions (Table 3). In the discussion, the results from the numerical simulations were compared to measured temperatures in wells.

The non-dimensional Nusselt number (Nu) and the recharge rate (R) were calculated to compare the results from different numerical models. Compared to conductive models, advective heat transport increased the total heat flux on the surface shown by the Nusselt number ($Nu = 1.23$–1.69). In the base model (M1), significant cooling effects were noticed due to topography-driven advective heat transfer beneath the recharge area of the western part, but this effect was less evident in the eastern part of the numerical model. At the main regional discharge area, which is located near the Danube River, a steady-state hot upwelling plume approaches the surface within a temperature range of $T = 70\,^\circ\text{C}$ and 80 °C. This result is consistent with the balneological features around Budapest, where several thermal spas have been established which are characterized by these highest temperatures. In the steady-state solutions, the calculated recharge rate was constant, $R = 157$ mm/yr, which is approximately half of the maximum recharge rate estimated from precipitation ($R/R' = 54\%$).

The superimposed effect of thermal buoyancy was evident from the non-dimensional Rayleigh and the modified Péclet numbers which were estimated at $Ra \approx 4700$ and at $Pe^* = 42.5$, respectively (Szijártó et al., 2019). Owing to the fully coupled mixed thermal convection, the numerical simulation led to a time-dependent, quasi-stationary (t>150 kyr) and weakly periodic solution. The time-dependence of the temperature field and hydraulic head was investigated in the Supplementary data (Appendix A). The

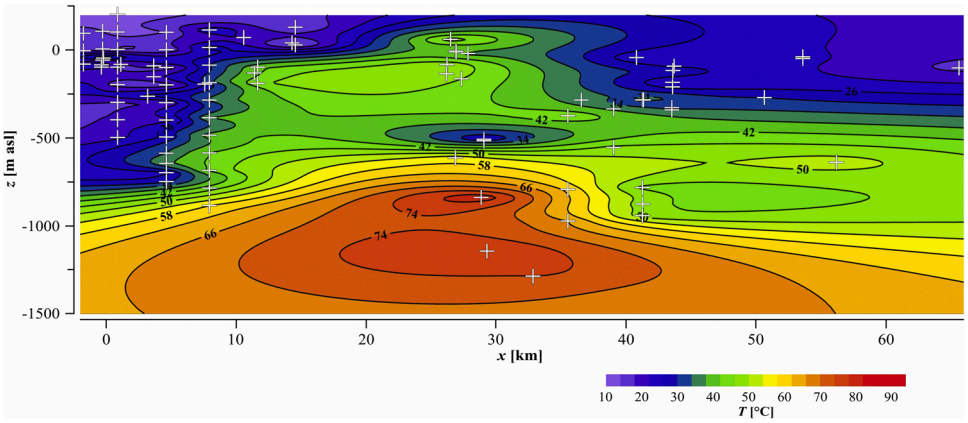

Fig. 13. 2D temperature field obtained from well observations (white crosses) located in the coordinate system of the numerical model (Fig. 1c). The vertical exaggeration is 13.5.

complementary effect of free thermal convection facilitated the evolution of hot upwelling from the thermal boundary layer, which intensified the heat and the mass flux compared to advective heat transport. Thus, the Nusselt number varied between $Nu = 1.56$ and 5.25, while the recharge rate was within a range of $R = 178$ mm/yr ($R/R' = 61\%$) (S3, M4a) and 250 mm/yr (86%) (S3, M1) (Fig. 9). By means of accessory scenarios, we investigated the effect of hydraulically conductive faults (M2) and radiogenic heat production within the hydrostratigraphic units (M3). As a conclusion, the studied natural features induce mainly local anomalies in the numerical model, their influence on the basin-scale groundwater flow pattern and the temperature field is not significant in the BTK. Finally, we tested the artificial effects of the boundary conditions prescribed along the bottom (M4a, M4b) and the side walls (M4c). It was established that neither the constant bottom temperature nor the constant heat flux is a perfect condition to imitate the nature of the real system. Using an 'internal' thermal condition (M4b) might be an appropriate method to minimize the artificial effect of the bottom boundary conditions. The studied boundary condition on the side walls can affect the temperature field and the flow pattern (M4c), especially near the boundaries, however, this effect causes only marginal changes in the main part of the numerical model.

Based on the comparison of the numerical results and the observation data (Dövényi, 1994; Mádl-Szőnyi et al., 2018; Mádl-Szőnyi, 2019), a weak, shallow advective 'cooling' effect is produced on the recharge area of the confined (eastern) side of the BTK (Fig. 13). However, the main heat transport mechanism is conductive due to the anisotropy of the Miocene hydrostratigraphic units, which can moderate the vertical flow in the deeper zones (z<-400 masl). Beneath the Danube River, a clear appearance of the advective heat transfer mechanism is noticed which was also supported by previous conceptional models and geochemical interpretations (Mádl-Szőnyi and Tóth, 2015; Mádl-Szőnyi et al., 2018; Mádl-Szőnyi, 2019; Máld-Szőnyi et al., 2019; Erőss, 2010; Erőss et al., 2012; etc.). Nevertheless, the superimposed buoyancy forces seem to be strong enough to induce time-dependent mixed thermal convection. The calculated geothermal gradients (Fig. 12), the negative temperature anomaly beneath the Danube River due to inclined hot plumes (Fig. 13) can be explained by the additional effect of free thermal convection. In addition, the quasi-periodic changes in both the temperature field and the hydraulic head distribution (Appendix A – Supplementary data) might explain the temperature and water level fluctuations observed from speleothems in caves of BTK (Virág, 2019).

In this basin-scale simulation, the cave systems and the preferential flow patterns caused by karstification, which are mainly located in the near-surface area, were neglected. However, the manifestations of karsification processes can be significant in local-scale flow systems. The isotropic approach is appropriate in the hydraulically conductive Triassic aquifers (HS8–HS10) using the EPM approximation. As a limitation of the model, the anisotropy of the hydraulic conductivity was neglected in the Neogene, Oligocene and Eocene hydrostratigraphic units (HS1–HS7). However, the changes in hydraulic conductivities were examined in Appendix A – Supplementary data.

Clearly, the numerical model outcomes substantial uncertainties caused due to e.g. the unknown physical properties of the hydrostratigraphic units, as the most hydrogeological models do (Mishra et al., 2009; Foglia et al., 2013; Song et al., 2015; etc.). Although, accomplishing a global sensitivity analysis (GSA) was not the purpose of the paper, influence of the hydraulic and the thermal conductivity was examined on the temperature field and on the monitoring parameters. It was established that the numerical results are influenced by the changes in hydraulic (K) and thermal (λ) conductivities, nevertheless, mixed thermal convection evolved in each numerical model within a range of analysed parameters (Appendix A – Supplementary data).

This study draws attention to the importance of different driving forces of groundwater flow, especially in deep carbonate sequences and adjoining sedimentary basins, such as the Buda Thermal Karst of Hungary. Globally, this hydrogeological situation is not unique as many other systems are also characterized by similar geological settings, for example the Upper Floridan aquifer system in west-central Florida, USA (Gulley et al., 2014), the Jinan karst aquifer system in east China (Wang et al., 2015), the Frasassi Anticline on the eastern slope of the Apennine mountain chain in Italy (Galdenzi et al., 2008), as well as the Black Hills in South Dakota, USA (Palmer and Palmer, 2000). The applied systematic numerical approach and thorough comparison of the numerical results and the observation data could improve understanding the interaction of the three heat transport mechanisms: heat conduction, advection and thermal buoyancy for specific hydrogeological environments.

CRediT authorship contribution statement

Márk Szijártó: Methodology, Software, Validation, Writing - original draft, Visualization. **Attila Galsa:** Methodology, Validation, Writing - review & editing, Supervision. **Ádám Tóth:** Data curation, Writing - review & editing. **Judit Mádl-Szőnyi:** Conceptualization, Writing - review & editing, Supervision.

Declaration of Competing Interest

The authors declare that they have no known competing financial interests or personal relationships that could have appeared to influence the work reported in this paper.

Acknowledgements

This research is part of a project that has received funding from the European Union's Horizon 2020 research and innovation program under grant agreement No 810980. The project was supported by the ÚNKP-19-3 and ÚNKP-19-4 New National Excellence Program of the Ministry for Innovation and Technology, by the Hungarian Scientific Research Fund (K 129279) and by the János Bolyai Research Scholarship of the Hungarian Academy of Sciences.

Appendix A. Supplementary data

Supplementary data associated with this article can be found, in the online version, at https://doi.org/10.1016/j.ejrh.2021.100783.

References

Abusaada, M., Sauter, M., 2012. Studying the flow dynamics of a karst aquifer system with an equivalent porous medium model. Groundwater 51 (4), 641–650. https://doi.org/10.1111/j.1745-6584.2012.01003.x.

Alföldi, L., 1981. A budapesti áramlási rendszer modellje (Modell of the geothermal flow system in Budapest). Hidrogeológiai Közlöny 61 (9), 397–403 (in Hungarian).

Alföldi, L., Bélteky, L., Böcker, T., Horváth, J., Korim, K., Liebe, P., Rémi, R., 1968. Budapest Hévizei (Thermal Water of Budapest). VITUKI, Budapest, p. 365 (in Hungarian).

An, R., Jiang, X.-W., Wang, J.-Z., Wan, L., Wang, X.-S., Li, H., 2015. A theoretical analysis of basin-scale groundwater temperature distribution. Hydrogeol. J. 23 (2), 397–404. https://doi.org/10.1007/s10040-014-1197-y.

Arola, T., Eskola, L., Jukka, H., Korkka-Niemi, K., 2014. Mapping the low enthalpy geothermal potential of shallow Quaternary aquifers in Finland. Geotherm. Energy 2 (9). https://doi.org/10.1186/s40517-014-0009-x.

Békési, E., Lenkey, L., Limberger, J., Porkoláb, K., Balázs, A., Bonté, D., Vrijlandt, M., Horváth, F., Cloetingh, S., van Wees, J.D., 2018. Subsurface temperature model of the Hungarian part of the Pannonian Basin. Glob. Planet. Change 171, 48–64. https://doi.org/10.1016/j.gloplacha.2017.09.020.

Berre, I., Doster, F., Keilegavlen, E., 2019. Flow and fractured porous media: a review of conceptual models and discretization approaches. Transp. Porous Media 130, 215–236. https://doi.org/10.1007/s11242-018-1171-6.

Bodri, L., 1981. Geothermal model of the Earth's crust in the Pannonian Basin. Tectonophysics 72, 61–73. https://doi.org/10.1016/0040-1951(81)90087-1.

Cathles, L.M., Smith, A.T., 1983. Thermal constraints on the formation of Mississippi Valley-type lead-zinc deposits and their implications for episodic basin dewatering and deposit genesis. Econ. Geol. 78 (59), 983–1002. https://doi.org/10.2113/gsecongeo.78.5.983.

Clauser, C., Villinger, H., 1990. Analysis of conductive and convective heat transfer in a sedimentary basin, demonstrated for the Rheingraben. Geophysis. J. Int. 100 (3), 393–414. https://doi.org/10.1111/j.1365-246X.1990.tb00693.x.

Csepregi, A., 2007. The effect of water withdrawal on the water balance of the Transdanubian range. In: Alföldi, L., Kapolyi, L. (Eds.), Mining-dewatering in the Transdanubian Range (in Hungarian). Geography Institute of Hungarian Academy of Science, Budapest, pp. 77–112. ISBN: 9789639545151.

Cserepes, L., Lenkey, L., 2004. Forms of hydrothermal and hydraulic flow in a homogeneous unconfined aquifer. Geophys. J. Int. 158 (2), 785–797. https://doi.org/10.1111/j.1365-246X.2004.02182.x.

Dobson, F.P., Timothy, J.K., Kneafsey, J., Hulen, J., Simmons, A., 2003. Porosity, permeability, and fluid flow in the Yellowstone geothermal system, Wyoming. J. Volcanol. Geotherm. Res. 123 (1-3), 313–324. https://doi.org/10.1016/S0377-0273(03)00039-8.

Domenico, P.A., Palciauskas, V.V., 1973. Theoretical analysis of forced convective heat transfer in regional ground-water flow. GSA Bull. 84 (12), 3803–3814. https://doi.org/10.1130/0016-7606(1973)84<3803:TAOFCH>2.0.CO;2.

Dövényi, P., 1994. Geophysical Characteristics of the Pannonian Lithosphere (in Hungarian). PhD Thesis. Eötvös Loránd University, Budapest, p. 127.

Dövényi, P., Horváth, F., 1988. A review of temperature, thermal conductivity and heat flow data for the Pannonian Basin. In: Horváth, F., Royden, L.H. (Eds.), The Pannonian Basin: A Study in a Basin Evolution. AAPG Memoir 45, 195–233. ISBN: 9781629811345.

Eppelbaum, L., Kutasov, I., Pilchin, A., 2014. Applied Geothermics, 1th ed. Springer-Verlag, Berlin Heidelberg, p. 751. ISBN: 978-3-642-34022-2.

Erhardt, I., Ötvös, V., Erőss, A., Czauner, B., Simon, S., Mádl-Szőnyi, J., 2017. Hydraulic evaluation of the hypogenic karst area in Budapest (Hungary). Hydrogeol. J. 25, 1871–1891. https://doi.org/10.1007/s10040-017-1591-3.

Erőss, A., 2010. Characterization of fluids and evaluation of their effects on karst development at Rózsadomb and Gellért Hill, Buda Thermal Karst, Hungary. Phd Thesis. Eötvös Loránd University, p. 171.

Erőss, A., Mádl-Szőnyi, J., Surbeck, H., Horváth, Á., Goldscheider, N., Csoma, A., 2012. Radionuclides as natural tracers for the characterization of fluids in regional discharge areas, Buda Thermal Karst, Hungary. J. Hydrol. 426, 127–137. https://doi.org/10.1016/j.jhydrol.2012.01.031.

Fodor, L., 2011. Geological sections across Budapest E-W. In: Mindszenty, A. (Ed.), Budapest: Geological Values and Man – Urbangeological Studies (in Hungarian). Eötvös Loránd University Press, Budapest, p. 20 (2013), ISBN: 9789632843681.

Foglia, L., Mehl, S.W., Hill, M.C., Burlando, P., 2013. Evaluating model structure adequacy: the case of the Maggia Valley groundwater system, southern Switzerland. Water Resour. Res. 49 (1), 260–282. https://doi.org/10.1029/2011WR011779.

Galdenzi, S., Cocchioni, M., Morichetti, L., Amici, V., Scuri, S., 2008. Sulfidic ground-water chemistry in the Frasassi caves, Italy. J. Cave Karst Stud. 70 (2), 94–107.

Garamhegyi, T., Székely, F., Carrillo-Rivera, J.J., Mádl-Szőnyi, J., 2020. Revision of archive recovery tests using analytical and numerical methods on thermal water wells in sandstone and fractured carbonate aquifers in the vicinity of Budapest, Hungary. Environ. Earth Sci. 79, 129. https://doi.org/10.1007/s12665-020-8835-6.

Ge, S., Garven, G., 1992. Hydromechanical modeling of tectonically driven groundwater flow with application to the Arkoma Foreland Basin. JGR Solid Earth 96 (B6), 9119–9144. https://doi.org/10.1029/92JB00677.

Goldscheider, N., Mádl-Szőnyi, J., Erőss, A., Schill, E., 2010. Review: thermal water resources in carbonate rock aquifers. Hydrogeol. J. 18 (6), 1303–1318. https://doi.org/10.1007/s10040-010-0611-3.

Gulley, J.D., Martin, J.B., Spellman, P., Moore, P.J., Screaton, E.J., 2014. Influence of partial confinement and Holocene river formation on groundwater flow and dissolution in the Florida carbonate platform. Hydrol. Process. 28 (3), 705–717. https://doi.org/10.1002/hyp.9601.

Haas, J., 1988. Upper Triassic carbonate platform evolution in the Transdanubian Mid-Mountains. Acta Geol. Hung. 31 (3-4), 299–312.

Haas, J., 2013. Geology of Hungary, 1th ed. Springer-Verlag, Berlin Heidelberg, p. 246. ISBN: 9783642219092.

Haas, J., Korpás, L., Török, Á., Dosztály, L., Góczán, F., Hámorné, V.M., Oraveczné, S.A., Tardiné, F.E., 2000. Upper Triassic basin and slope facies in the Buda Mts.–Based on study of core drilling Vérhalom tér, Budapest (in Hungarian with English abstract). Földtani Közlöny 130 (3), 371–421.

Haas, J., Budai, T., Csontos, L., Fodor, L., Konrád, G., Koroknai, B., 2014. Explanation to the Pre-cenozoic Geological Map of Hungary (in Hungarian). Geological and Geophysical Institute of Hungary, Budapest, p. 71. ISBN: 9789636712983.

Harrison, W.J., Summa, L.L., 1991. Paleohydrology of the Gulf of Mexico basin. Am. J. Sci. 291, 109–176. https://doi.org/10.2475/ajs.291.2.109.

Havril, T., 2018. Numerical Simulation of Groundwater Flow and Heat Transport over Geological Time Scales at the Margin of Unconfined and Confined Carbonate Sequences. PhD Thesis. Eötvös Loránd University, p. 90.

Havril, T., Molson, J.W., Mádl-Szőnyi, J., 2016. Evolution of fluid flow and heat distribution over geological time scales at the margin of unconfined and confined carbonate sequences - A numerical investigation based on the Buda Thermal Karst analogue. Mar. Pet. Geol. 78, 738–749. https://doi.org/10.1016/j.marpetgeo.2016.10.001.

Jiang, X.W., Wan, L., Wang, X.S., Wang, D., Wang, H., Wang, J.Z., Zhang, H., Zhang, Z.Y., Zhao, K.Y., 2018. A multi-method study of regional groundwater circulation in the Ordos Plateau, NW China. Hydrogeol. J. 26 (5), 1657–1668. https://doi.org/10.1007/s10040-018-1731-4.

Kaiser, B.O., Cacace, M., Scheck-Wenderoth, M., Björn, L., 2011. Characterization of main heat transport processes in the Northeast German Basin: constraints from 3-D numerical models. Geochem. Geophys. Geosyst. 12 (7), 1–17. https://doi.org/10.1029/2011GC003535.

Kaiser, B.O., Cacace, M., Scheck-Wenderoth, M., 2013. 3D coupled fluid and heat transport simulations of the Northeast German Basin and their sensitivity to the spatial discretization: different sensitivities for different mechanisms of heat transport. Environ. Earth Sci. 70 (8), 3643–3659. https://doi.org/10.1007/s12665-013-2249-7.

Kovács, J., Müller, P., 1980. A Budai-hegységek hévizes tevékenységének kialakulása és nyomai. Karszt és Barlang 2, 93–98.

Lapwood, E.R., 1948. Convection of a fluid in a porous medium. Math. Proc. CPS 44 (4), 508–521. https://doi.org/10.1017/S030500410002452X.

Lenkey, L., 1993. Study of thermal anomaly at Tiszakécske by numerical modelling of thermal convection (in Hungarian with English abstract). Magyar Geofizika 34 (1), 30–46.

Lenkey, L., Dövényi, P., Horváth, P., Cloetingh, S.A.P.L., 2002. Geothermics of the Pannonian basin and its bearing on the neotectonics. EGU Stephan Mueller Special Publication Ser. 3, 29–40.

Licour, L., 2014. The geothermal reservoir of Hainaut: the result of thermal convection in a carbonate and sulfate aquifer. Geol. Belg. 17 (1), 75–81.

Lipsey, L., Pluymaekers, M., Goldberg, T., van Oversteeg, K., Ghazaryan, L., Cloetingh, S., van Wees, J.-D., 2016. Numerical modelling of thermal convection in the Luttelgeest carbonate platform, the Netherlands. Geothermics 64, 135–151. https://doi.org/10.1016/j.geothermics.2016.05.002.

Long, J.C.S., Remer, J.S., Wilson, C.R., Witherspoon, P.A., 1982. Porous media equivalents for networks of discontinuous fractures. Water Resour. Res. 18 (3), 645–658. https://doi.org/10.1029/WR018i003p00645.

Lopez, T., Antoine, R., Kerr, Y., Darrozes, J., Rabinowicz, M., Ramillien, G., Cazenave, A., Genthon, P., 2016. Subsurface hydrology of the Lake Chad Basin from convection modelling and observations. Surv. Geophys. 37, 471–502. https://doi.org/10.1007/s10712-016-9363-5.

Mádl-Szőnyi, J., 2019. Pattern of Groundwater Flow at the Boundary of Unconfined and Confined Carbonate Systems on the Example of Buda Thermal Karst and its Surroundings (in Hungarian). DSc Thesis, p. 150.

Mádl-Szőnyi, J., Tóth, Á., 2015. Basin-scale conceptual groundwater flow model for an unconfined and confined thick carbonate region. Hydrogeol. J. 23, 1359–1380. https://doi.org/10.1007/s10040-015-1274-x.

Mádl-Szőnyi, J., Tóth, Á., 2017. Topographically driven fluid flow at the boundary of confined and unconfined sub-basins of carbonates: basic pattern and evaluation approach on the example of Buda thermal Karst. In: Renard, P., Bertrand, C. (Eds.), EuroKarst 2016, Neuchâtel: Advances in Karst Science. Springer, Cham, pp. 89–98. https://doi.org/10.1007/978-3-319-45465-8_10.

Mádl-Szőnyi, J., Erőss, A., Tóth, Á., 2017. Fluid flow systems and hypogene Karst of the Transdanubian range, Hungary–With Special emphasis on Buda thermal Karst. In: Klimchouk, A., Palmer A, N., De Waele, J., Auler, A.S., Audra, P. (Eds.), Hypogene Karst Regions and Caves of the World. Cave and Karst Systems of the World. Springer, Cham, pp. 267–278. https://doi.org/10.1007/978-3-319-53348-3_17.

Mádl-Szőnyi, J., Erőss, A., Havril, T., Poros, Zs., Győri, O., Tóth, Á., Csoma, A., Ronchi, P., Mindszenty, A., 2018. Fluids, flow systems and their mineralogical imprints in the Buda Thermal Karst (in Hungarian with English abstract). Földtani Közlöny. 148, 71–96.

Magri, F., 2009. Derivation of the Coefficients of Thermal Expansion and Compressibility for Use in FEFLOW (implementation Code in C++). White Paper III: WASY GmbH. Institute for Water Resource Planning and System Research, Berlin, pp. 13–23.

Máld-Szőnyi, J., Czauner, B., Veronika, I., Tóth, Á., Sinom, Sz., Erőss, A., Bodor, P., Havril, T., Boncz, L., Sőreg, V., 2019. Confined carbonates? – regional-scale hydraulic interaction or isolation? Mar. Pet. Geol. 107, 591–612. https://doi.org/10.1016/j.marpetgeo.2017.06.006.

Malkovsky, V.I., Magri, F., 2016. Thermal convection of temperature-dependent viscous fluids within three-dimensional faulted geothermal systems: estimation from linear and numerical analyses. Water Resour. Res. 52 (4), 2855–2867. https://doi.org/10.1002/2015WR018001.

Marosi, S., Somogyi, S., 1990. Magyarország kistájainak katasztere. Geography Institute of Hungarian Academy of Science, Budapest, p. 89. ISBN: 9637395091.

Mersich, I., Práger, T., Ambrózy, P., Hunkár, M., Dunkel, Z., 2003. Climate Atlas of Hungary (in Hungarian). Hungarian Meteorological Service, Budapest, p. 107. ISBN: 9637702830.

Mishra, S., Deeds, N., Ruskauff, G., 2009. Global sensitivity analysis techniques for probabilistic ground water modeling. Ground Water 5, 727–744. https://doi.org/10.1111/j.1745-6584.2009.00604.x.

Nield, D.A., Bejan, A., 2017. Convection in Porous Media, 5th ed. Springer Int., p. 988 ISBN: 9783319495613.

Noack, V., Scheck-Wenderoth, M., Cacace, M., Schneider, M., 2013. Influence of fluid flow on the regional thermal field: results from 3D numerical modelling for the area of Brandenburg (North German Basin). Environ. Earth Sci. 70, 3523–3544. https://doi.org/10.1007/s12665-013-2438-4.

Palmer, A.N., Palmer, M.W., 2000. Speleogenesis of the Black Hills Maze Caves, South Dakota, USA. In: Klimchouck, A.B., Ford, D.C., Palmer, A.N., Dreybrodt, W. (Eds.), Speleogenesis. Evolution of Karst Aquifers. National Speleological Society, Huntsville, pp. 274–286.

Pasquale, V., Chiozzi, P., Verdoya, M., 2013. Evidence for thermal convection in the deep carbonate aquifer of the eastern sector of the Po Plain, Italy. Tectonophysics 594, 1–12. https://doi.org/10.1016/j.tecto.2013.03.011.

Przybycin, A.M., Scheck-Wenderoth, M., Schneider, M., 2017. The origin of deep geothermal anomalies in the German Molasse Basin: results from 3D numerical models of coupled fluid flow and heat transport. Geotherm. Energy 5 (1), 1–28. https://doi.org/10.1186/s40517-016-0059-3.

Rabinowicz, M., Boulègue, J., Genthon, P., 1998. Two- and three-dimensional modeling of hydrothermal convection in the sedimented Middle Valley segment, Juan de Fuca Ridge. J. Geophys. Res. 103 (B10), 24045–24065. https://doi.org/10.1029/98JB01484.

Rman, N., Tóth, Gy., 2011. T-JAM Vízföldtani koncepcionális modell (in Hungarian), p. 25.

Scanlon, B.R., Mace, R.E., Barrett, M.E., Smith, B., 2003. Can we simulate regional groundwater flow in a karst system using equivalent porous media models? Case study, Barton Springs Edwards aquifer, USA. J. Hydrol. 276, 137–158. https://doi.org/10.1016/S0022-1694(03)00064-7.

Sehgal, S., 1973. Groundwater Resources of Punjab State - a Recens Study. CBI and P Annual Research Session May, pp. 1–23.

Simmons, C.T., Narayan, K., Wooding, R.A., 1999. On a test case for density-dependent groundwater flow and solute transport models: the Salt Lake Problem. Water Resour. Res. 35 (12), 3607–3620. https://doi.org/10.1029/1999WR900254.

Song, X., Zhang, J., Zhan, C., Xuan, Y., Ye, M., Xu, C., 2015. Global sensitivity analysis in hydrological modeling: review of concepts, methods, theoretical framework, and applications. J. Hydrol. 523, 739–757. https://doi.org/10.1016/j.jhydrol.2015.02.013.

Szijártó, M., Galsa, A., Tóth, Á., Mádl-Szőnyi, J., 2019. Numerical investigation of the combined effect of forced and free thermal convection in synthetic groundwater flow basins. J. Hydrol. 572, 364–379. https://doi.org/10.1016/j.jhydrol.2019.03.003.

Tari, G., Báldi, T., Báldi-Beke, T., 1993. Paleogene retroarc flexural basin beneath the Neogene Pannonian Basin: a geodynamic model. Tectonophysics 226 (1), 433–455. https://doi.org/10.1016/0040-1951(93)90131-3.

Tóth, J., 2009. Gravitational Systems of Groundwater Flow: Theory, Evaluation, Utilization. Cambridge University Press, United Kingdom, p. 297. ISBN: 978–0–521–88638–3.

Tóth, Á., 2018. Groundwater Flow Systems and Hydraulic Connection of the Bakony–Balaton Highland–Lake Balaton Region (in Hungarian). PhD Thesis. Eötvös Loránd University, p. 169.

Tóth, J., Almási, I., 2001. Interpretation of observed fluid potential patterns in a deep sedimentary basin under tectonic compression: hungarian Great Plain, Pannonian Basin. Geofluids 1, 11–36. https://doi.org/10.1046/j.1468-8123.2001.11004.x.

Vendel, M., Kisházi, P., 1964. Összefüggések melegforrások és karsztvizek között a Dunántúli-középhegységben megfigyelt viszonyok alapján. MTA Műszaki Tudományok Osztály Közleménye 32, 393-417, 33, 205-234.

Virág, M., 2019. Hypogene and epigene karstic processes and their influence on the evolution of the Rózsadomb caves in Buda – by the examples of Szemlő-hegy Cave and Molnár János Cave (in Hungarian). PhD Thesis. Eötvös Loránd University, p. 318.

Voss, C.I., Simmons, C.T., Robinson, N.I., 2010. Three-dimensional benchmark for variable-density flow and transport simulation: matching semi-analytic stability modes for steady unstable convection in an inclined porous box. Hydrogeol. J. 18 (1), 5–23. https://doi.org/10.1007/s10040–009–0556–6.

Wang, J., Jin, M., Jia, B., Kang, F., 2015. Hydrochemical characteristics and geothermometry applications of thermal groundwater in northern Jinan, Shandong, China. Geothermics 57, 185–195. https://doi.org/10.1016/j.geothermics.2015.07.002.

White, F.M., 1988. Heat and Mass Transfer. Addison-Wesley Publishing Company, USA, p. 736. ISBN-13: 9780201170993.

Yang, J., Large, R.R., Bull, S.W., 2004. Factors controlling free thermal convection in faults in sedimentary basins: implications for the formation of zinc-lead mineral deposits. Geofluids 4 (3), 237–247. https://doi.org/10.1111/j.1468-8123.2004.00084.x.

Yang, J.W., Feng, Z.H., Luo, X.R., Chen, Y.R., 2010. Numerically quantifying the relative importance of topography and buoyancy in driving groundwater flow. Sci. China Earth Sci. 53 (1), 67–71. https://doi.org/10.1007/s11430-009-0185-x.

Zimmermann, W.B.J., 2006. Multiphysics Modeling With Finite Element Methods. World Scientific Publishing Company, Singapore, p. 422. ISBN: 9812568433.